REPORT DOCUMENTATION PAGE

Form Approved
OMB NO. 0704-0188

Public reporting burden for this collection of information is estimated to average 1 hour per response, including the time for reviewing instructions, searching existing data sources, gathering and maintaining the data needed, and completing and reviewing the collecting of information. Send comment regarding this burden estimates or any other aspect of this collection of information, including suggestions for reducing this burden, to Washington Headquarters Services, Directorate for information Operations and Reports, 1215 Jefferson Davis Highway, Suite 1204, Arlington, VA 22202-4302, and to the Office of Management and Budget, Paperwork Reduction Project (0704-0188), Washington, D.C. 20503.

1. AGENCY USE ONLY *(Leave blank)*	2. REPORT DATE 4/13/98	3. REPORT TYPE AND DATES COVERED Final Progress / January 1995 - February 1998

4. TITLE AND SUBTITLE Active Materials for Photonic Systems (AMPS)	5. FUNDING NUMBERS
6. AUTHOR(S) Lawrence E. Pado	DAAH04-95-C-0007

7. PERFORMING ORGANIZATION NAMES(S) AND ADDRESS(ES) The Boeing Company MC1021310 P.O. Box 516 St. Louis, MO 63166	8. PERFORMING ORGANIZATION REPORT NUMBER ST-98-02

9. SPONSORING/MONITORING AGENCY NAME(S) AND ADDRESS(ES) U.S. Army Research Office P.O. Box 12211 Research Triangle Park, NC 27709-2211	10. SPONSORING/MONITORING AGENCY REPORT NUMBER ARO 33523.1-MS

11. SUPPLEMENTARY NOTES
The views, opinions and/or findings contained in this report are those of the author(s) and should not be construed as an official Department of the Army position, policy or decision, unless so designated by other documentation.

12a. DISTRIBUTION / AVAILABILITY STATEMENT Approved for public release; distribution unlimited.	12b. DISTRIBUTION CODE

19980521 097

13. ABSTRACT *(Maximum 200 words)*

The AMPS program has created the first 3-axis MEMS active fiber optic micro-aligner, which will allow for in-package alignment or fiber optic and micro-optic components. The micro-aligner is a wafer level fabricated device, based on a combination of silicon micromachining and LIGA technology. The electrically controllable actuators demonstrate the high force and displacement necessary to overcome fiber optic cable, counterforce springs, friction, and wirebonds to perform in-package alignment of a fiber optic. AMPS has demonstrated movement of >20 microns in all three axes in an in-package configuration. The first prototype device are currently small enough (4 X 4 X 0.5 mm3) to fit into a standard 14 pin butterfly package. Future devices with the same forces and displacements can be made smaller than 1 X 1 X 0.5 mm3 thus allowing for multiple single mode fiber optic attachments inside a standard opto-electronic package.

The AMPS program has developed a FEM design/analysis tool. This program allows for fully coupled analysis of elecro-thermo-mechanical properties. This program runs on Windows NT machines and comes complete with a User's Manual.

14. SUBJECT TERMS MEMS, micro-actuation, single mode, fiber optics, alignment, PZT, LIGA, FEM	15. NUMBER OF PAGES 78
	16. PRICE CODE

17. SECURITY CLASSIFICATION OR REPORT UNCLASSIFIED	18. SECURITY CLASSIFICATION OF THIS PAGE UNCLASSIFIED	19. SECURITY CLASSIFICATION OF ABSTRACT UNCLASSIFIED	20. LIMITATION OF ASTRACT UL

NSN 7540-01-280-5500   Enclosure 1

Standard Form 298 (Rev. 2-89)
Prescribed by ANSI Std. 239-18
298-102

Active Materials for Photonic Systems (AMPS)

Final Progress Report

Authors

Lawrence E. Pado
John Haake
Herb Smith
Rob Wood (MCNC)
Orlando Auciello (Argonne)

Reporting Period

January 1995 – February 1998

U.S. Army Research Office

Contract Number

DAAH04-95-C-0007

Institution

Lawrence E. Pado
The Boeing Company
P.O. Box 516 (MC S1021310)
St. Louis, MO 63166-0516
Phone: (314) 232-1069
Fax   : (314) 777-1171
lawrence.e.pado@boeing.com

DTIC QUALITY INSPECTED 2

Table of Contents

List of Appendixes, Illustrations, and Tables

Executive Summary

Figure 1 – High Power Laser Systems Concepts

The objective of the Active Materials for Photonic Systems (AMPS) program is to develop and demonstrate the wafer level processing of active materials needed to manufacture smart electro-mechanical structures and devices leading to an active fiberoptic connector (AFC). The inexpensive, lightweight alignment of large numbers of single mode optical fibers is an enabler for defense applications such as high power diode pumped lasers for directed energy systems (Figure 1), photonically controlled phased array radars and fiber optic based sensor systems. Each of these systems requires transmission of optical energy or signals through single mode optical fibers in order to maintain precise phase relationships. Connection of single mode optical fiber requires alignment tolerances of 0.1 to 0.3 microns, about ten times more precisely than can be accomplished with passive alignment techniques.

To develop the AFC devices, this program had to overcome two major obstacles. First, the feature sizes needed range from 10^{-5} to 10^{-3} meters. As shown in Figure 2, this range falls in a gap between the capabilities of the well established technologies of Very Large Scale Integrated (VLSI) circuits and standard precision machining. The processes
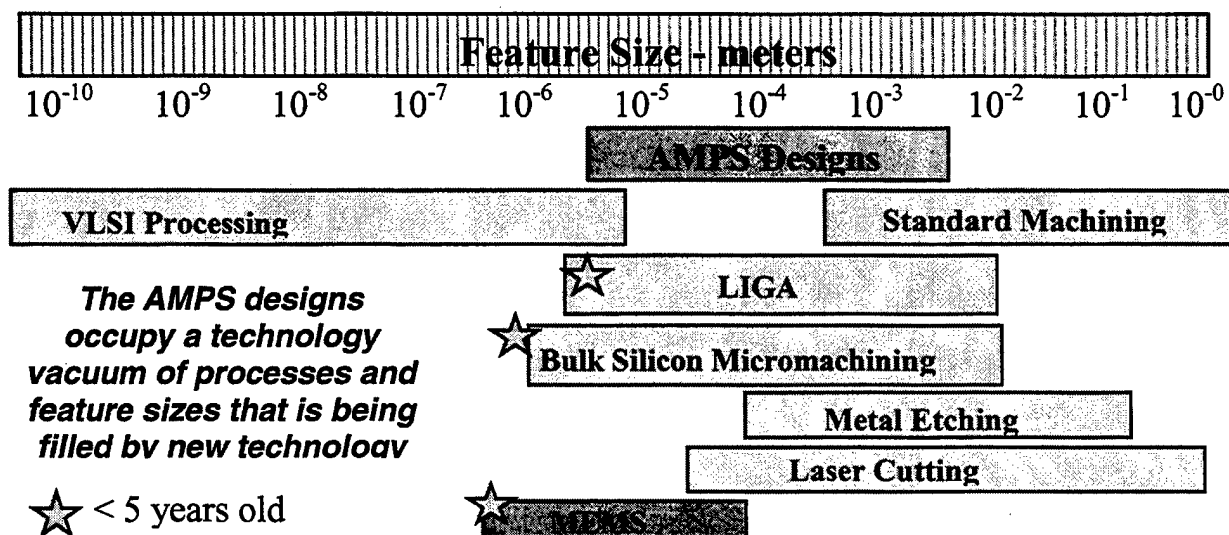
Figure 2 – Device Feature Size and Manufacturing Processes

needed to produce feature sizes in this range have only recently been enabled by some of the newest manufacturing technologies such as bulk silicon micromachining, LIGA (a German acronym referring to lithography, plating, and molding), and Micro-Electro-Mechanical Systems (MEMS). The second major obstacle to the development of AFC devices was that the required forces and displacements are one to two orders of magnitude larger than available from current MEMS actuators. The feature size obstacle was overcome by developing the ability to combine LIGA and bulk silicon micromachining. The force/displacement obstacle was overcome by the use of a proprietary thermal actuator developed at MCNC in Research Triangle Park, NC.

Nickel LIGA Thermal Actuators

Although the AMPS program had begun by exploring the use of piezoelectric materials such as PZT (lead-zirconium-titanate) to provide the actuation, it become apparent that achieving a three-axis PZT actuator would require a major breakthrough in deposition of these materials. Thermal bimorph (nickel/silicon) bending actuators were found to have up to ten times more available work per unit volume than the best ferroelectric ceramics. In addition, a thermal actuator fabricated from only one or two materials, one etched and the other deposited, is much easier to affordably fabricate in a production environment.

Program Accomplishments

The AMPS program demonstrated the first high force and high displacement, in-plane, two-axis fiber optic aligner in 1996. In 1997 we demonstrated the third axis using a nickel/silicon thermal bimorph actuator, see Figure 3. The resulting AFC can provide three-axis alignment of optical fibers over an alignment range of at least ten microns in all axes, with a device small enough to fit inside a standard Photonic butterfly package.
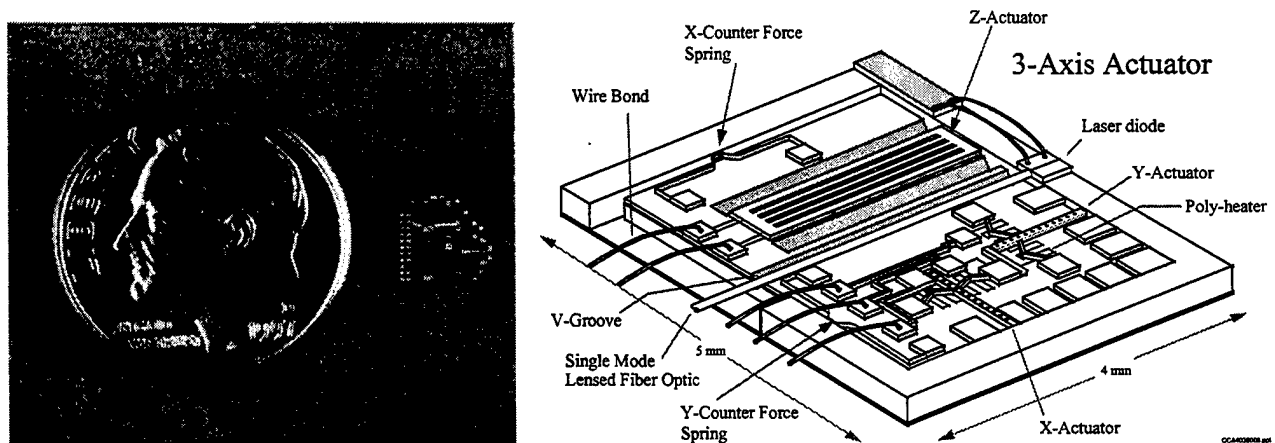
Figure 3 – The AMPS three-axis active fiberoptic aligner

2

Statement of the Problem Studied

Objectives of the Active materials for Photonic Systems Program

The overall objective of the Active Materials for Photonic Systems (AMPS) program was to develop and demonstrate the wafer level processing of active materials needed to manufacture smart electro-mechanical structures and devices, using an active fiberoptic connector (AFC) as a development process vehicle. A co-objective was to create a fully coupled thermal-electrical-mechanical finite element (FEM) based design tool to help develop the AMPS connector. These goals have been met and can provide a simple, inexpensive means of interconnecting photonic devices such as fiber optic cables, laser diodes, and photonic chips, allowing for the rapid growth of the photonics market.

Overall Program Summary

The overall objective of the Active Materials for Photonic Systems (AMPS) program was to develop and demonstrate the wafer level processing of active materials needed to manufacture smart electro-mechanical structures and devices, using an active fiberoptic connector (AFC) as a development process vehicle. This objective was chosen due to the severe difficulty of aligning single mode fiber optic cable to other cables or to other photonic devices such as laser diodes. The difficulty lies in the very small feature sizes under consideration, which are on the sub-micron level. Figure 4 illustrates the magnitude of the problem. Figure 1A shows a 125μm fiber laying along side the 'D' of a Lincoln penny. Figure 4B shows the 5μm light-conducting core of the fiber. For another size reference, Figure 4C shows the eye of a small garden ant. Figure 4D is a close up of the eye showing that it is made up of eyelets approximately 10 to 15μm in diameter. Alignment of the single mode fiber cores to tolerances of 0.1 to 0.3 microns is required to achieve acceptable coupling efficiency.

Working with feature sizes and processes in this range is difficult and requires the use of the newest manufacturing technologies. Over recent years these technologies have begun to fill a vacuum in manufacturing technology. Figure 5 shows the how the AMPS device feature size fits in comparison to technologies such as VLSI processing and standard machining. As can be seen in the figure, newer technologies such as bulk silicon micromachining, LIGA, and MEMS technology in general all provide pathways to the creation of AMPS devices.
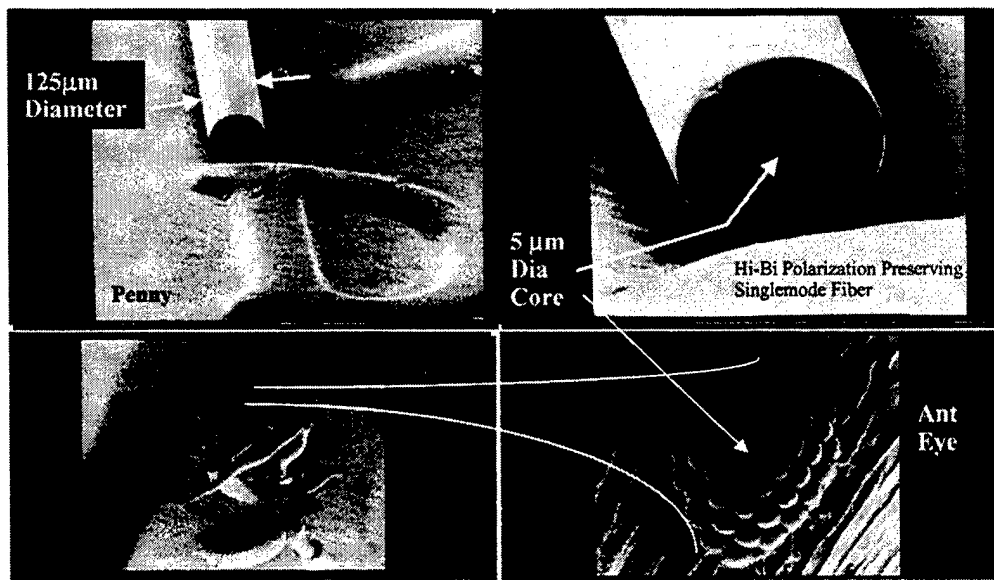
Figure 4 – Illustration showing the relative size of a single mode fiber core

The AMPS designs occupy a technology vacuum of processes and feature sizes that is being quickly filled by new technology

★ < 5 years old
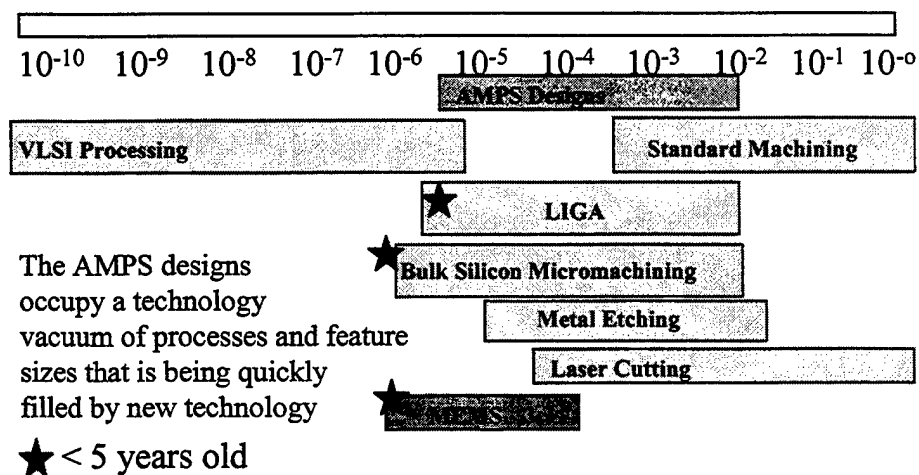
Figure 5 – A comparison of manufacturing processes with respect to feature size

Although multi-mode fiber, with alignment tolerances of several microns functions well for data communications, single mode fiber is required for several significant defense applications. For example, Figure 6 shows many defense programs for laser based attack and defense applications such as theatre ballistic missile defense, the AF Fotofigher concept, and ground based and ship based missile defense.

Applications such as these will need sophisticated photonics backplane interconnect systems using single mode optical fiber, which are not practical to assemble unless IPMA type devices are used. Other applications such as photonic based phased array radar and

fiber optic based bragg grating sensors are enabled by the inexpensive alignment of single mode fiber optics.
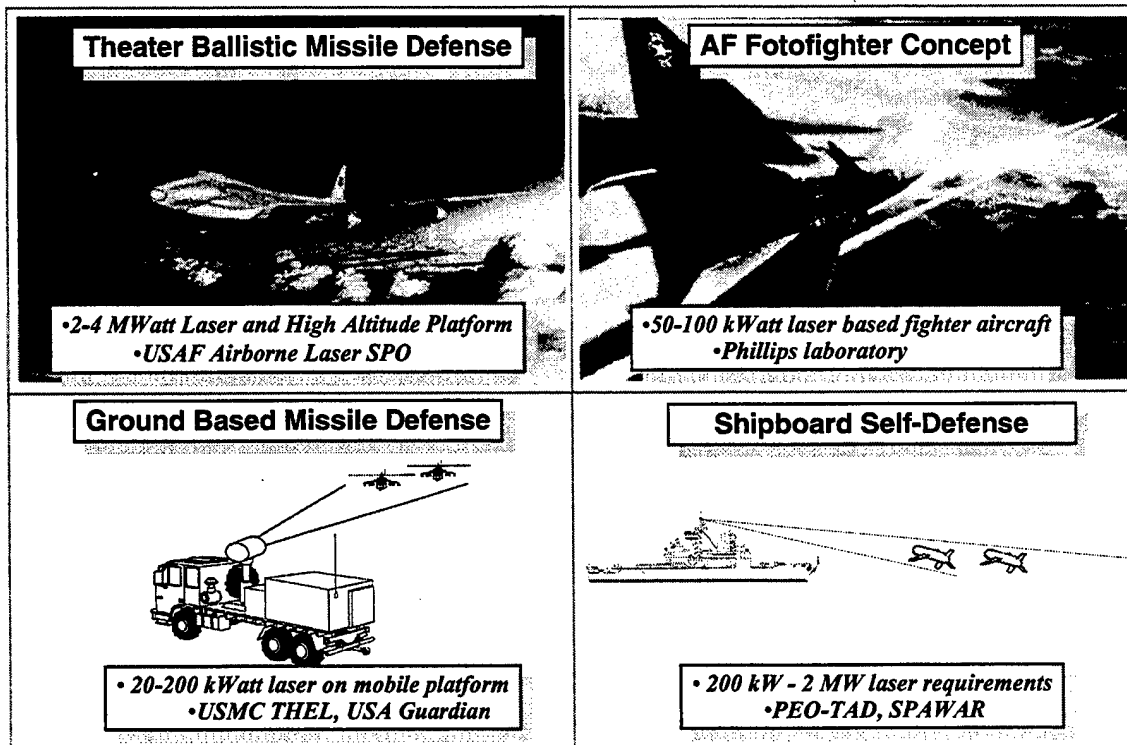
Figure 6 - Advanced Military Systems Requiring Single mode Fibers

Sol-Gel PZT

Due to the potential benefits of single mode fiber optic based optical systems, the AMPS program was created to bring these types of devices into reality. The program initially approached the program solely from a PZT/PMNA based active material perspective. The challenge was both to create a high quality, consistent PZT formula, and then integrate it into a MEMS production environment.

The forces and displacements required to move a fiberoptic cable requires thick PZT and bulk micromachined silicon structures. There are several major barriers that have to be broken through to achieve a 3 axis PZT MEMS actuator small enough to fit into opto-electronic packages:

1. Fabrication of thick PZT layers from 1.5µm to 10µm
2. PZT compatible wafer level fabrication processes such as silicon bulk micromachining and in some cases surface micromachining had to be developed. Etchants for PZT had to be developed, and processes for etching silicon structures while leaving the PZT unharmed also had to be developed

5

3. A PZT deposition process that is tolerant of surface morphology, such as vertical walls, so as to achieve in-plane actuators had to be developed.

The initial subcontractor for the PZT/MEMS development was MetaTek. Many PZT based options were evaluated: Sol-Gel PZT, organically modified PZT co-studied by MetaTek and Sandia National Labs, and tape cast PZT developed by Dr. Wayne Huebner of the University of Missouri, Rolla. Even looking at all of these technologies, it became clear that MetaTek did not have the ability to further integrate PZT with bulk micromachining. MetaTek achieved working material on 4 inch silicon wafers with reasonable thickness, 1.1 microns, but the material had very poor morphology, cracks, that would never survive a silicon MEMS fabrication process.

At this point the AMPS program found it prudent to examine alternate means of actuation to be co-developed due to the very difficult problems associated with the use of PZT in a production environment. In the second phase of the AMPS program, Boeing subcontracted with MCNC due to their PZT expertise and world-renowned MEMS fabrication expertise (MUMPS and HI-MEMS).

Although it was clear that it was possible to create out-of-plane motion on a diaphragm based on past work that MCNC had done, it was going to be very difficult to lay down PZT on a vertical plane to achieve in-plane actuation and thus achieve full three axis control. In order to successfully achieve the forces and displacements necessary to achieve in-plane actuation, the PZT would have to be deposited in bulk micromachined trenches. To address this, Orlando Auciello of MCNC worked with Maryland University to achieve laser deposition of PZT. This process produced PZT films that were independent of surface morphology but were not compatible with 4 inch silicon wafers without major capital investment. Therefore the only deposition option near-term was Sol-Gel deposition of PZT. Even though this would not overcome the 3D barrier and yield a 3 axis actuator, there were many firsts that would evolve from the fabrication of thick Sol-gel PZT / bulk micromachined silicon MEMS devices. MCNC successfully produced spectrally reflective 1.1 micron thick standard Sol-gel PZT films. This was done after significant improvement of the spinning environment and the annealing equipment. In addition to this, multiple adhesion metals were examined to find those that were compatible with the production process and also provided good adhesion properties.

CVD PZT

In approximately mid-1997, the AMPS program heard of the unique Chemical Vapor Deposition [CVD] of single crystal PZT capability at Argonne National Labs [ANL] under the direction of Dr. Chris Foster. Orlando Auciello who was the AMPS PZT Principle Investigator at MCNC took a research position at ANL with Foster. Upon consultation Dr's. Susan Trolier-McKinstry of Penn State -MRL, Foster, and Auciello of ANL, it was determined that CVD deposition of PZT was the only process that would be able to break through the major barriers to achieve 3-axis PZT actuators.

1. CVD has the capability to produce thick films with fabrication times similar to Sol-gel PZT
2. CVD is compatible with silicon MEMS fabrication processes
3. CVD is Surface morphology independent. It is the only process that has a chance in depositing PZT on vertical sidewalls

Argonne capability in Mid - 1997 consisted of only a horizontal reactor which deposited CVD on small 1 cm ^{2} samples. 4 inch wafer capability required an investment to which both Argonne and the AMPS program contributed. The use of 4 inch silicon wafers required the building of a vertical CVD reaction chamber with both liquid and solid precursor sources. As is discussed later in this report, this reactor is nearly complete, and it has been shown that PZT can indeed be deposited on vertical side walls.

Nickel LIGA Thermal Actuators

By Mid-1996 it had become apparent that achieving a 3-axis PZT actuator would require a major breakthrough in deposition of PZT. The AMPS program started to look at other more manufacturable methods of making a 3-axis actuator. Research revealed that thermal bimorph [nickel/silicon] has more available work per unit volume than the best bulk PZT. A thermal actuator being fabricated of only two materials, one etched and the other deposited, is orders of magnitude easier to fabricate. MCNC has a program with DARPA -ETO known as the HI-MEMS alliance. For a minimal fee anyone can make nickel LIGA test structures. While funding negotiations were underway, MCNC on their own made springs and precision alignment structures. MCNC also developed the TAB actuator, which proved to be the actuator of choice.

AMPS Success

Six months after MCNC was under contract, the AMPS program demonstrated the first ever, high force and high displacement LIGA in-plane thermally actuated 2 axis fiber optic aligner. Almost one year later we have demonstrated a third axis using a final nickel/silicon thermal actuator, see Figure 7. This actuator allows for full three axis alignment and has been received very well in the laser/optics community. Boeing and MCNC have signed a memorandum of agreement for commercialization and are actively seeking partners for commercialization.
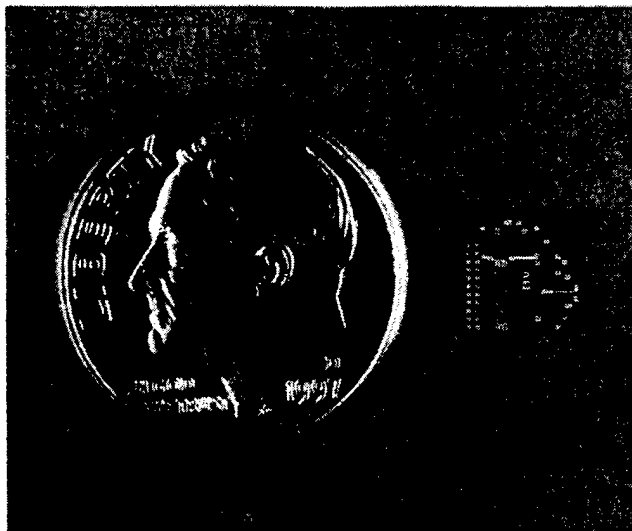
Figure 7 – The final AMPS three axis device

Background on Fiber Alignment

Packaging dominates the cost of OE devices

The packaging of individual single mode opto-electronic components currently dominates the product cost in excess of 40-50% [1, 2]. The development of high volume, lower cost opto-electronic manufacturing technologies must take place in order to accelerate the installation of opto-electronics in lower speed and shorter distance networks. These include telecommunications wavelength division multiplexing [WDM] and computer and video applications for both defense and commercial systems. [3, 4] One of the principle reasons we do not see more applications of all-optical (photonic) [5,6,7,8] and single mode opto-electronics in the consumer and military marketplace is the lack of reliable, cost effective and easily implemented single mode fiber optic alignment and bonding to discrete opto-electronic and photonics devices.

Boeing and MCNC have developed a fully integrated Microelectromechanical (MEMS) fiber optic aligner that is small enough to fit into a standard opto-electronic hermetic package. The In-Package Micro-Aligner [IPMA] is a novel device that utilizes proprietary actuator technology to achieve both large forces and displacements. The IPMA eliminates the current bottleneck in the manufacturing of fiber pigtailed optical circuits by putting the alignment robot into the package. The IPMA will free the opto-electronic engineer from the costs and constraints associated with the packaging of photonic circuits, and allow for the use of maximum performance devices.

Present Technology

Optoelectronics is a hybrid technology based on the integration of lasers of InP, GaAs or In_xGa_{1-x}, detectors, silicon ICs, and GaAs high frequency circuits [9] and then finally coupled to the outside world with silica fiber optics. The opto-electronic designer must utilize hybrid integration of these individual components so as to take advantage of the

8

maximum performance obtained from the respective foundries: GaAs, InP, $In_xGa_{1-x}As$, Silicon, and SiO_2.

The laser-to-fiber coupling is the weakest link in the opto-electronic hybrid manufacturing process, and its costs are driving the design of the components and packaging to the detriment of individual component performance. High single mode coupling efficiency is achieved by mode matching the laser to the fiber. There are two approaches to this problem: match the waveguide modes or lens coupling. Without a lens to mode match the waveguide to the fiber, the waveguide mode shape must be made symmetric to match the fiber and must be well confined to minimize propagation and scattering losses. Confinement and mode shape are coupled and generally cannot both be optimized without sacrificing device performance [10]. Lens coupling offers mode matching without changing the laser or the fiber optic but at the price of significantly tightened tolerances (lensed fiber optics) or multiple lens elements.

Most of the future high-speed digital applications will require an isolated laser module in order to minimize intensity and phase noise. These systems require an even more demanding alignment of separate lenses to collimate the laser beam through an isolator and then to focus this back into a fiber optic [11]. There are many benefits to increased coupling and reduced feedback, however this requires more antireflection coated optical components that have to be precisely aligned.

If one can design with external in-line fiber optic isolators, a lensed fiber optic is very desirable due to component reduction. Anti-reflection coated hyperbolic lensed fiber optics can offer up to 100% coupling efficiency to all guided wave devices [12,13] with significant reduction in optical feedback reflections. This coupling gain comes with a loss in the area of fiber optic alignment tolerances. For 1300 nm systems, instead of 2 –3 microns for 3 dB loss for butt coupled connection, the lensed fiber optic tolerances are now 0.5- 0.75 microns [14, 15]. This is reduced even further for a polarization preserving system and by the ratio of the wavelengths for shorter wavelength systems. While 2-3 micron tolerances are achievable with passive alignment between micro-machined surfaces, the much tighter alignment tolerances require an active alignment system.

Alignment

The problem still to be solved is the need to align optical components and fiber optics with submicron ($<1 \times 10^{-6}$ m) precision in less than 0.1 minute, with the cost per aligned fiber optic significantly less than the device to be pigtailed. The photonics engineer is currently constrained by these single mode laser-to-fiber coupling/packing issues. The fiber pigtailing process has to be automated significantly to reduce the costs. Lawrence Livermore National Labs put together a simple model - Figure 8) [16] that shows substantial costs savings upon automation. However, the automation of the opto-electronic industry requires alignment tolerances that far exceed the current electronics industry requirements for part placement. In addition, for this automation to be cost effective the process of opto-electronic parts handling will have to be addressed.
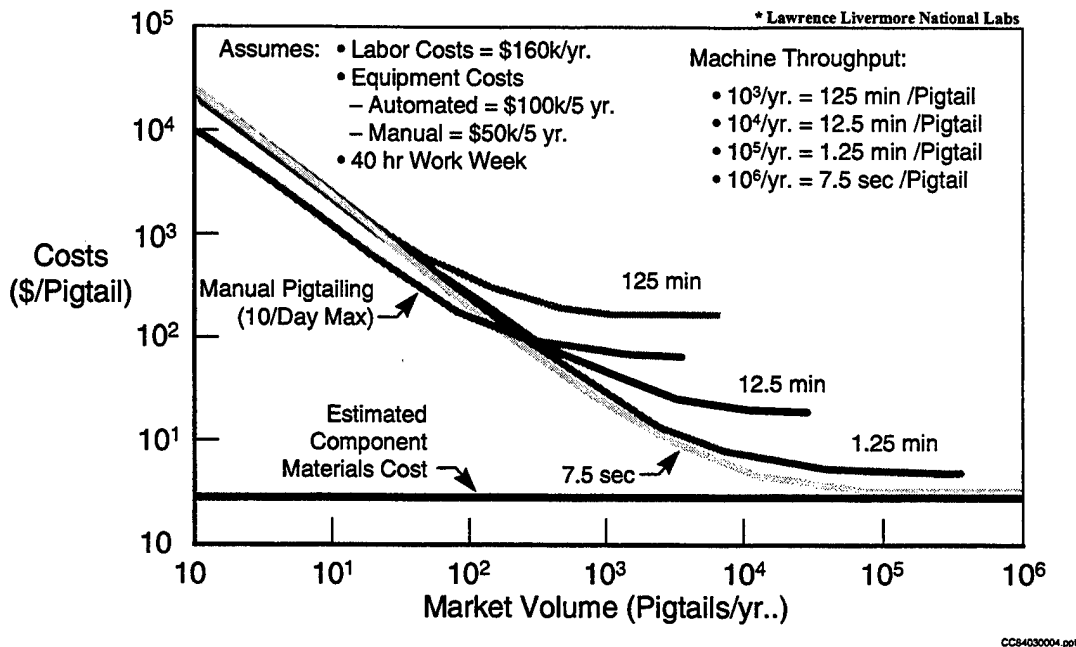
Figure 8 - Simplified Cost model showing savings upon automation.

Active Alignment

Active alignment systems use machine vision to place the fiber to within a few microns and then measure coupled power to achieve final alignment to the waveguide. The current automated systems are package and device specific. Like any fabrication machine, it requires different and expensive fixtures and tooling to precisely hold packaging and to position and bond the coupled fiber. There is no opto-electronic equivalent for part handling such as tape feed and pick-and-place machines. The loading and operating of the automated fiber pigtailing machines currently takes as long or longer as the alignment. Some have addressed these using kit trays with loaded fibers that are conveyed to the fine alignment area. [17]

Passive alignment

Spurred by the demands of the telecommunication industry for the high density packaging of single mode laser diode arrays and their connection to fiber optical arrays and WDM systems, [18] advances have been made in packaging single mode opto-electronic devices with passive alignment. The focus has been on the idea of using micromachined silicon benches as first proposed in 1975 [19] with passive alignment techniques: Silicon V-grooves with patterned metallization and passive alignment structures [20]. Other techniques are using LIGA structures, [21] Flip chip with solder surface tension during reflow to move and align piece parts [22]. These techniques are claiming +/- 1-micron alignment tolerances and in some cases, optical coupling efficiency for cleaved fibers as good as actively aligned components. However, several studies have identified the sources of lateral and transverse misalignment and have related these to the variations in the micromachined components, assembly and thermo-mechanical stresses. These studies have shown laser diode to optical fiber transverse and lateral misalignments of

10

approximately 2.8 microns for single mode coupling[23, 24]; clearly these are not suitable for single mode fiber optic alignment and packaging.

Background on Finite Element Analysis Tools

Finite element methods have been available for some time and have become a standard approach to the solution of problems in solid mechanics. Their utility in other fields has grown considerably in recent years with the extension of the approach to problems in fluid dynamics, diffusion, electric and magnetic field analysis. The bulk of the commercially available codes, however, remain focused on problems in solid mechanics. Other areas are frequently the topics of research programs and technical papers.

ABAQUS and NASTRAN are two of the better-known commercial finite element codes. They both offer a wide range of element types and analysis procedures. Piezoelectric analysis is handled differently by each of these codes. ABAQUS addresses it explicitly with the inclusion of a piezoelectric element. Whereas this allows coupling of the electrical and mechanical degrees of freedom, the element does not allow the thermal degrees of freedom to be included in the analysis. Thermal stress problems can also be handled, which again only represents 2/3 of the problem. At the time the piezoelectric analysis was implemented in ABAQUS, the fully coupled behavior was not considered by HKS (the developers of ABAQUS) as having sufficient market value to justify the effort to include it in the code.

NASTRAN has been the quintessential standard in finite element analysis codes for some twenty years now. It also handles primarily problems in solid mechanics. Thermal stress problems are a standard part of their analysis repertoire. Piezoelectric analysis cannot be done directly, however. Piezoelectric behavior can be simulated to some extent by treating it as a thermal stress problem and contriving a set of thermal expansion coefficients that emulate the piezoelectric behavior. This is very approximate, however, since the thermal behavior cannot fully represent the piezoelectric coupling. This is obvious in that the matrices characterizing their effects are of different order. In addition, if you are simulating the piezoelectric behavior with the thermal characteristics, then the thermal behavior cannot be included in the analysis.

The fully coupled theory has been developed in the literature for some time, so the solution to the situation was to develop a small, special purpose code that would provide an element with the complete coupling. Mesh generation codes were written for several of the problems to be studied. These codes allowed for the description of the problem parametrically, and for the use of nodes and elements generated from these parametric descriptions, ready for input to the finite element code. This is generally the big job in preparing the input to the code and these mesh generation codes allowed for the study of the problems parametrically in a very efficient way once the initial generation code was in place.

Background and summary of PZT Diaphragm Creation

The AMPS PZT effort at MCNC was directed in the application of PZT piezoelectric materials to fiber alignment. The effort was oriented toward developing sol-gel deposition and metallization processes which would be integratable with established MEMS fabrication processes. This was an extension of previous efforts at MCNC in applying PZT to ink-jet devices. This work was summarized in a MCNC internal technical report titled "Fabrication of Prototype Thin-Film Ink-Jet Devices", dated September 3, 1991, with authors: Mark Walters, John Clarke, Gary Jones, Orlando Auciello, John Standish, and Tena Standish. The objective the AMPS PZT effort was to merge PZT processing capability with bulk silicon micromachining in MCNC's 4-inch facility to support future production of PZT actuators.

A key task was developing the sol-gel precursor formulations and techniques for building usable layer thicknesses having the correct crystallographic form for optimal piezoelectric properties. Tooling and materials were procured and successfully applied to fabricating PZT layers up to 1.0μm thickness with good piezoelectric properties. Additionally, metallization techniques were investigated to determine the best approach to integrating the PZT layers in real devices. The PZT portion of the AMPS program at MCNC was successful in establishing sol-gel deposition and metallization processes yielding high-quality PZT layers. Further development in the area of design and process integration will be required to fully exploit this material as an actuator for fiber alignment.

Summary of the Most Important Results

LIGA BASED IN PACKAGE ACTIVE MICRO ALIGNER

The LIGA In-Package Micro Aligner (IPMA), developed under the AMPS program, is a fully integrated 3-axis micro aligner, which we believe is the first of its kind. It is small enough (5 X 4 X 0.5 mm³) to fit into current electro-optic packages. In this design, MEMS technology allows the alignment robot to be attached to the fiber optic. This literally moves the fiber pigtailing robot from outside to inside the package. There have been several papers published on the use of MEMS actuators to actively align and move fibers. The actuator types published were based on electromagnetic, [25, 26] shape memory alloy, [27, 28] thermal [29], electrostatic, [30, 31] and piezoelectric.[32] This technology has not garnered the attention of the industry because they are large MEMS devices, not fully integrated, or have high power requirements.

The IPMA devices are micromachined silicon chips, which possess both mechanical and electronic functionality. Such devices are fabricated using silicon processing adapted from integrated circuit manufacturing for which a broad base of infrastructure and expertise exists. The actuator requirements are shown in Table 1.

Size	< 5 mm² x 0.5 mm
Displacement	> 10 microns in one direction
Force	> 10 mN
Power	< 1.0 watt

Table 1 - Actuator Specifications

In order to meet these specifications, a specific MEMS technology, nickel surface micromachining, was targeted for the IPMA application. This process combines nickel active structures fabricated via the LIGA technique (German acronym which refers to lithography, plating, and molding) with surface-micromachined silicon control devices. A single chip 5 mm on a side may contain 10's to 100's of active nickel structures controlled by an equivalent number of silicon circuits. The IPMA MEMS chip contains three active nickel subsystems employed as microactuators to achieve three-axis control of the attached fiber. The MEMS chip is thus the interface between the fiber and the coupled device.

As shown Figure 9 and Figure 10, the single mode fiber is passively aligned to the actuators and reference structures through use of either silicon V-grooves or electrodeposited reference structures. Since all structures are formed via microlithographic patterning, the accuracy of their placement relative to each other is limited only by the accuracy of the photomask patterning tool. Today's microlithography equipment will provide better than 0.2 μm placement accuracy, which is more than adequate for the IPMA approach. Microactuators on the chip act on either an internal fiber support stage, or on external reference structures defined in the package made with

the same process as that of the actuator. In both cases the actuators must produce sufficient force to overcome constraining forces of the bending of the fiber, counterforce springs, friction, wirebonds, and the weight of the chip itself. Using proprietary actuator technology developed at MCNC's MEMS Technology Applications Center, the chip and its attached fiber and wirebonds are literally pushed into position to align the fiber with its coupled device, and held in place during bonding.
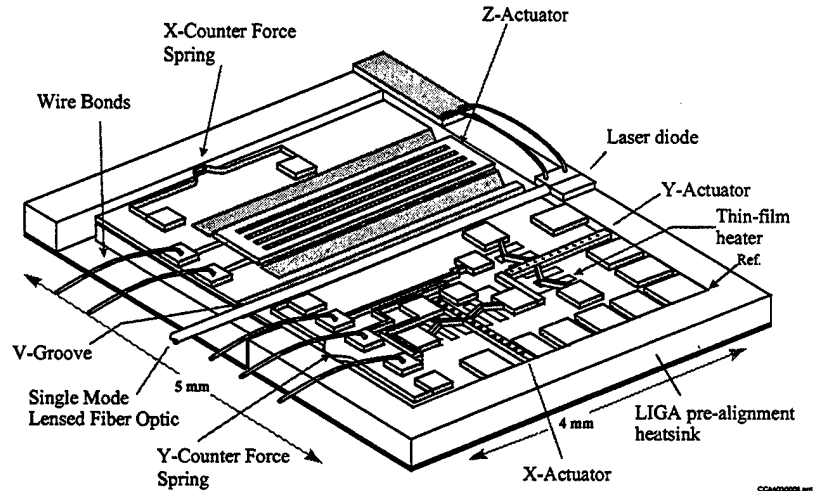
Figure 9 -Unmounted 3-axis In-package Micro Aligner
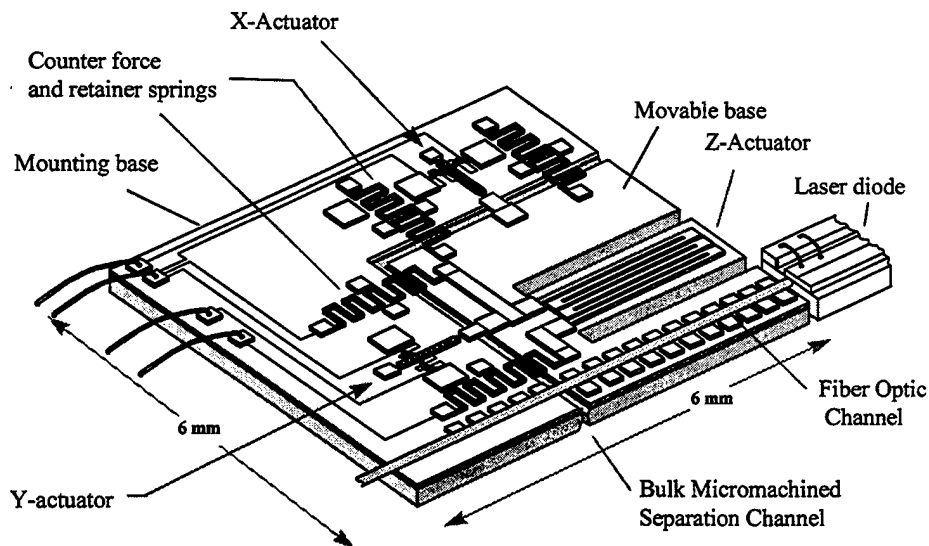
Figure 10 - Mounted 3-axis in-package micro aligner

14

IPMA Fabrication Process Description

Fabrication of the IPMA chip begins with deposition of the plasma enhanced chemical vapor deposition [LPCVD] silicon nitride layer on silicon which is later etched via bulk etching to form the moving silicon micropositioning stage. A low-stress LPCVD silicon nitride layer, patterned on both sides of the wafer, is used for this purpose. This stage is released in a later step via bulk silicon etching. Surface micromachined layers are then patterned to form the thermal isolation structures and microheaters for the thermal actuators. Several photolithographic patterning steps are required to define the nitride layers, heater layer, and sacrificial layer. This is accomplished with standard cleanroom processing. A thick 60uM electroplated nickel layer is patterned using the LIGA technique. See Figure 11 for basic outline of this fabrication process. This step relies upon synchrotron-based deep x-ray lithography provided by the Center for Advanced Microstructures and Devices (CAMD) at Louisiana State University, Baton Rouge, LA.
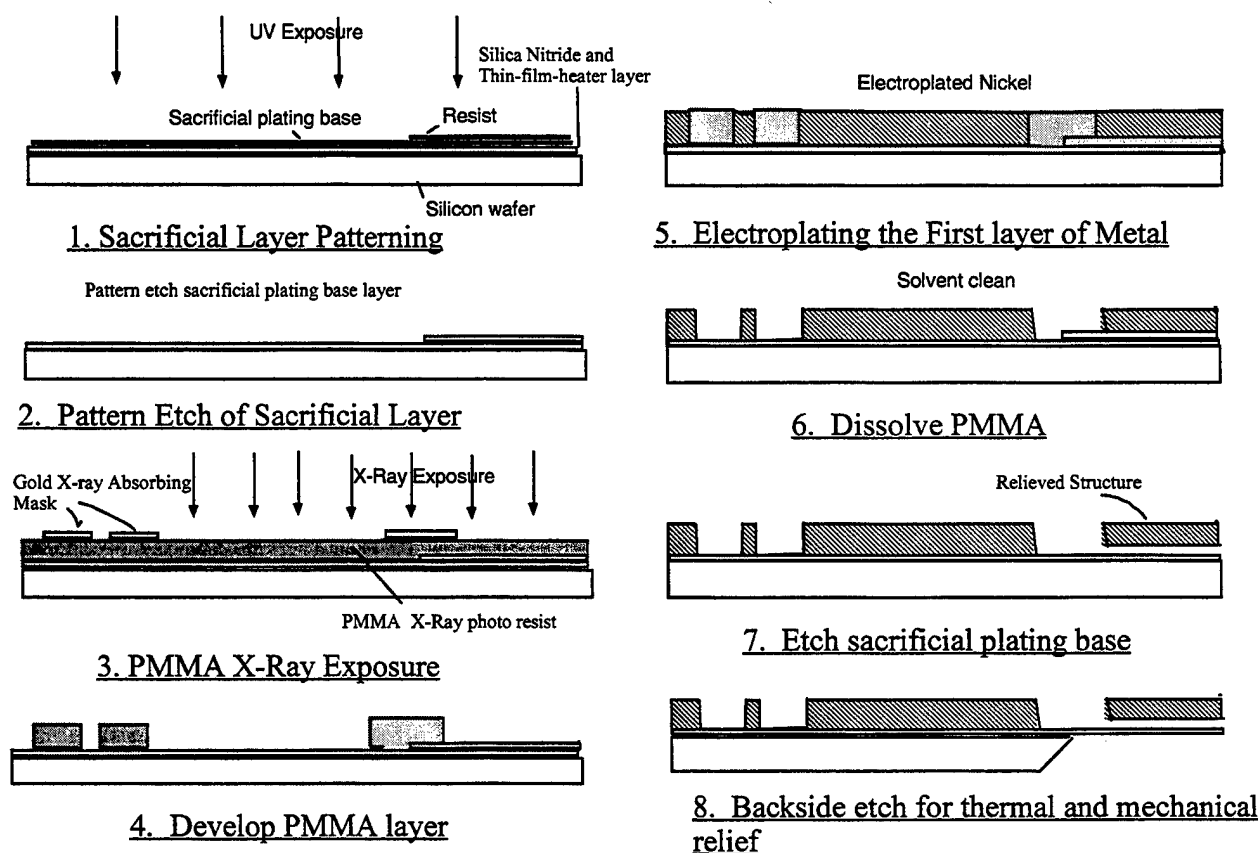
Figure 11 - LIGA Basic Outline of process for making IPMA devices

A key aspect of LIGA patterning is the ability to define high aspect ratio structures, which is crucial for obtaining actuation in the plane of the IPMA chip and for defining corresponding spring structures with high in-plane compliance and high out of plane stiffness. LIGA also permits plating heights which are sufficiently thick to form passive fixturing guides for the fiber, precise edge reference structures, and provides convenient definition of conductor paths for actuator control input. Optical lithography guarantees

15

excellent alignment of reference structures with the fiber guides and thereby provides assembly alignment accuracy within the capture range of the microactuators.

Following LIGA patterning, the movable portions of the nickel structure are released via sacrificial etching. The silicon is then subjected to anisotropic etching to cut away the stage portion of the IPMA chip and thermally relieve the poly-silicon heaters, using the silicon nitride layer as an etch mask. At this point the stage [Figure 10] is suspended by nickel springs defined in the LIGA layer and is responsive to positioning via the three microactuators. All told, there are five mask levels including the x-ray step. The resulting process merges surface and bulk silicon micromachining with nickel surface micromachining via the LIGA technique. Following wafer-level fabrication, the devices are singulated using conventional dicing, packaged in a butterfly-type flatpack with the fiber optic pigtail and the photonic device it is to be aligned with, and powered via conventional wirebonds.

Prototype Fabrication

On the way to creating the final AMPS IMPA devices, a series of prototypes first had to be created. The following discussion is illustrative of the techniques for creating similar devices.

Two-axis Device:

Fabrication of two prototypes was performed. The first device was a two-axis aligner using orthogonal actuators to push on reference structures in order to move a fiber within a 20μm alignment range . Two approaches were taken to defining the reference structures. In the first, referred to as internal references, these structures were part of the chip itself, and consisted of pin sockets which could be mated with a second substrate having pins placed approximately 4mm apart. Holes etched in the AFMA chip allow the pins to pass through the backside of the chip and mate with LIGA pin socket on the frontside. The Pin socket is attached to the substrate through folded spring structures also fabricated via LIGA. These springs were designed to counteract the actuators and stabilize the aligner. X and Y actuators pushing on the socket frame causes the entire chip to move with respect to the fixed pin substrate. With a fiber fixed in the v-groove, actuation control is achieved in two axis as the chip slides on the base substrate.

The second referencing technique made use of external reference structures. The concept here is to mate the AFMA chip with a second substrate having precisely defined orthogonal walls for the actuator to bear against. The device to be aligned with the fiber would be placed within 10μm of its target location within this second substrate, and the actuators would provide the final alignment. This external referencing scheme required high-precision definition of the AFMA chip edge compared with the internal reference approach, since initial alignment of the fiber would be directly determined by edge placement uncertainty. A new chemical scribing technique was used to achieve this precision.

In chemical scribing, the edge of the chip is defined though lithography and etching rather than by sawing. Etched borders defined at the same time as the fiber v-groove and

other structures serve as perforations to permit segmentation of the completed wafer into individual chips by cleavage along the perforations. LIGA structures projecting slightly beyond the etched edge become the new mechanical edge of the chip. Since these structures are fabricated at the same time as the actuators, registration between them is nearly perfect.

Prototypes of both internally and externally referenced AFMA devices were successfully fabricated and performed as expected. This represented the first integration of conventional silicon micromachining with sacrificial LIGA, and validated a number of new processing techniques, such as chemical scribing discussed above. Based on the success of this first prototype, a second prototype was designed which incorporated a third axis of control.

Three axis device:

Fabrication of the second prototype fiberoptic aligner was performed during the final six months of the project. This prototype includes a third axis of control achieved with a nickel-silicon thermal bimorph used in conjunction with in-plane actuators. As with the first prototype, fabrication was a combination of silicon surface and bulk micromachinining and nickel micromachining via X-Ray LIGA. Heaters were fabricated using resistive elements defined via surface micromachining. Bulk etching was used to define regions of silicon that carries the fiber and which forms the moveable microstage to be manipulated with the actuators during active fiber alignment. A key element of this prototype is the nickel-silicon bimorph used to manipulate the z-axis adjustment. Several designs of this actuator were fabricated and tested. Typical designs are depicted in Figure 9 and Figure 10.

The z-actuator resembles a diving board and consists of 60μm of electroplated nickel deposited over a 50μm thick silicon cantilever, which is fixed at one end. An insulated resistive layer is interposed between the nickel and silicon to form the heater. The free end of the cantilever has a section of full-thickness silicon which acts as a "boss" to bear against the chip mount and raise the stage in response to heating. Several designs of the z-actuator were successfully tested, with better than expected results. With 300 mW of electrical input, the actuators produce more than 100μm of vertical deflection. Linear motion of the fiber support stage was confirmed, i.e. motion was confined to the z-axis, with little translation in x and y.

Processing issues prevented testing of all three axis at once. Marginal adhesion of the x and y anchor structures caused loss of anchor and bearing integrity. Also, a step coverage problem caused loss of integrity of x and y polysilicon heaters. The anchor problem was addressed with use of an alternative plating base layer structure. This change makes the anchor-substrate interface immune to undercutting effects of the sacrificial etch step. A mask redesign was performed to implement this change. The step coverage issue was fixed by masking the wafer frontside during bulk backside etching. Combining these changes permitted fabrication of functional devices, which are still undergoing testing. The few processing issues, which arose during this prototype run, appear to be easily correctable with minor changes in the design layout and process

sequence. Results with this prototype has provided validation of the overall MEMS approach and shows a viable commercial path for product development with this technology.

Cost

The first prototypes cost approximately $20 to $25 dollars each. These are only a few hundred devices amortized over the prototype nonrecurring costs. Although actuator designs are not optimized, the forces and deflections were shown to be several times larger than required. The most real estate is taken up by the anisotropic bulk micromachining etching to thermally isolate the heaters and release the out-of-plane actuator. These wafer real-estate requirements can be reduced by using reactive ion etching which can achieve through wafer etching with aspect rations of 40:1.[33] The optimized actuator will be on the order of 1 mm^2 meaning 1000's of IPMA's per wafer. With the low recurring fabrication costs these devices can easily achieve unit prices of a few cents.

LIGA TESTING PROCEDURES AND RESULTS

Experimental Considerations

In order to develop a method to measure the force and displacement, behavior of LIGA-MEMS devices must be considered. The specific attributes include: device geometry, anticipated force, and displacement behavior. The heights of LIGA-MEMS structures may be on the order of 20 to 200 microns with planar dimensions ranging from tens of microns to millimeters. The estimated forces required to deflect the structures range from 10 to 10$_m$N. The anticipated deflections range from 10 to 100's of microns.

Passive and active devices were studied. Measurement of passive devices involved deflecting the device a known amount with a calibrated mechanical probe. Measurement of active devices involved energizing the active device, measuring displacement produced and then measuring the force by using the calibration to initially move the device towards the re-energized position.

LIGA-MEMS Devices

- Heights on the order of 20 to 200 microns
- Anticipated deflections 10 to 100's of microns
- Estimated forces (simple beam) 10 μN to 100 mN
- Active and Passive devices

At the beginning of this effort there were no fully integrated MEMS actuators that could produce the Displacement [>10 microns] and the forces [> 10 mN] necessary for in-package alignment. Since MEMS is a relatively immature technology there are no metrology standards for measuring and characterizing these structures. We have developed an inexpensive yet accurate means of measuring force and displacement of LIGA micro springs and actuators by using a calibrated cantilevered fiber optic beam as a

force probe. This method has a large dynamic range from 10 micro-Newtons to 100's of milli-Newtons with accuracies of a few percent.

Displacement Measurement

The measurement of the displacement of a micromachine is fairly straightforward. A high power microscope, such as shown in Figure 12, has several objective lenses (5X to 40X) giving a magnification range of 50X to 400X. This, along with a translation stage and a graduated microscope eyepiece, provides displacement measurement. The translation stages [x,y,z] are equipped with electronic vernier scales which gives a reading to within +/- 1 micron. By using the focus in the Z-axis for high power objective, one can measure vertical height to approximately 5 microns. The actuator is powered and the stages are moved to reposition the target point in the cross hair. The resulting displacement is recorded from the stage displacement readout. For out of plane displacement, the objective can be refocused and the change in vertical height can be recorded.
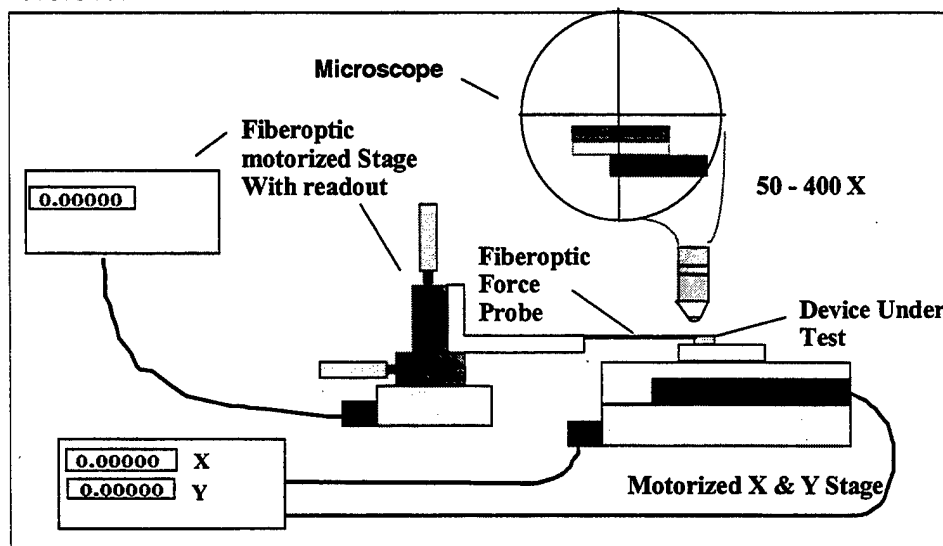
Figure 12 - MEMS micro-actuator force and displacement characterization set-up

As shown in Figure 13 for two different actuators the displacement is fairly linear at 60-70 microns/W. At ~0.45 watts the actuator has a displacement of over ~30 microns. The out-of-plane silicon/nickel bimorph was qualitatively characterized to have a displacement of >120 microns at 0.3 watts.
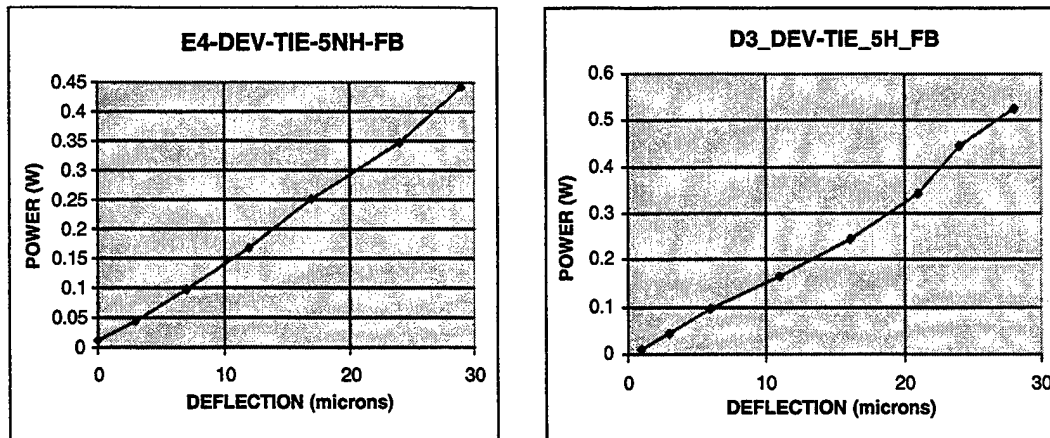
Figure 13 - In-plane thermal actuator displacement versus power

Force Measurement

Fiberoptic Probe

In order to measure force, a MEMS compatible force probe was needed. For a force probe, the AMPS program used a simple, calibrated cantilevered beam made from pure silica SiO_2, a well-characterized material. The beam is made from commonly available optical telecommunication fiber. This provides a long and slender rod that can be held at a distance and still probe a device under test. In addition, the fiberoptic tip can be easily melted and shaped (hook or point) such that it can access hard to get at devices in the middle of a wafer.

Telecommunication fiberoptic is a excellent choice due to the tolerances required by the industry. Since the optical loss is highly dependent on the quality of the fiber material, the batch to batch fiber material uniformity is only matched by the semiconductor wafer industry. Therefore, we have a manufacturing process that produces kilometers of fiber of the same diameter and material. The diameter of the single mode fiber has to be maintained to micron tolerances so as to fit into the fiberoptic connector and ferrules. These requirements have driven the manufacturing process such that the uniformity of a fiberoptic is to within a 1% of diameter from batch to batch. For this particular application where small sections of fiber are used the uniformity is much less than 1%. Degradation of the fused silica happens when the pure silica is exposed to moisture. Therefore, to maintain long-term repeatability the fiber has to be hermetically jacketed. The jacket material used for the fiberoptic probes described here was a high temperature polyimide. There are other hermetic materials that are strongly recommended due to their inherent hermeticity. Spectran makes a fiberoptic with Carbon Pyrocoat ®, and Fiberguide Industries makes aluminum coated fibers. These coatings provide a chemical bond with the silica and prevent water induced damage to the fiber.

The fiberoptic probe of a given length has to be held very rigidly to get the ideal boundary condition at the base. A very hard construction epoxy was used to mount the fiber inside steel tubing. A selection of probes were produced to provide a range of force properties. A block with hole and set screw was made to allow for quick change out of fiberoptic probes.

Some devices to be tested, specifically surface micromachined devices, have a very low profile (<10 μm) which a round 140 μm diameter fiber would roll over. This problem can be overcome by tailoring the tip of the fiber with a fiberoptic fusion splicer. See Figure 14. This allows one to create hook and points that protrude from the shank of the fiber.
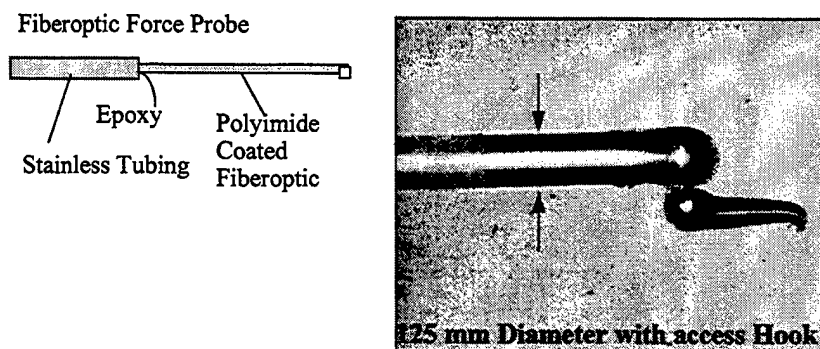
Figure 14 - Picture of fiberoptic Probe (Artist) and actual probe with special tip

Simple Beam Theory

The Force versus deflection for a Fiberoptic cantilevered beam can be simply described with the following equation (5, 6).

$$F = \frac{x \cdot \delta \cdot 3 \cdot E_s \, I_T}{(L)^3} \cdot 10^6 \quad \text{micro newtons}$$

Where L is the length of the cantilevered beam, δ is the tip deflection in meters, and E_s and I_T are the modulus of elasticity for fused silica and moment of inertia for the transformed beam. Where I_T for the composite beam is refer to strength of Materials text if appropriate:

$$I_T = \frac{(EI)_{silica} + (EI)_{polyimide}}{E_{Silica}} \quad \text{Where: } (EI)_{Polyimide} = E\left(I_{\substack{outer \\ radius}} - I_{\substack{inner \\ radius}}\right)$$

and

21

$$I := \frac{\pi \cdot R^4}{4}$$

Where E_s for Fused silica is 73 GPa (6) and the E for polyimide is nominally 3.2 GPa. The effect from the jacket material is a small percentage of the effective silica beam stiffness, $E_s I_s$. In our case the fibers that we used were 140/125 and 275/240 μm jacket /glass diameter polyimide coated fiberoptics. The polyimide only adds ≅3% to the total Beam stiffness. In Table 2 some off-the-shelf fibers and the associated parameters are listed:

Poly coated Fiber	EI Glass (N* m^2)	EI Polyimide (N* m^2)	Total (N* m^2)
140 J /125-G	$8.75*10^{-7}$	$2.2*10^{-8}$	$8.97*10^{-7}$
275-J/240-G	$11.89 * 10^{-6}$	$3.8* 10^{-6}$	$12.3 *10^{-6}$
750-J/720-G	$9.63 * 10^{-4}$	$7.5*10^{-6}$	$9.70*10^{-4}$

Table 2 - Calculated Beam Stiffness of sample fiberoptic diameters

Calibration

The predicted beam stiffness was verified by empirically measuring the amount of force the tip of the fiber exerted while its base was displaced. The set-up for this is shown in Figure 3, in which a precision scale with an accuracy of +/- 4.9 μN is used to measure the force, and a precision stage with micrometer readout was used to measure the displacement of the base. The resulting curve for the 275/240 polyimide coated fiberoptic is shown in Figure 15. A calculated EI value for the fiber beam was 12.2 X 10^{-6} N*m^2 which agrees well with the predicted value shown in Table 2.
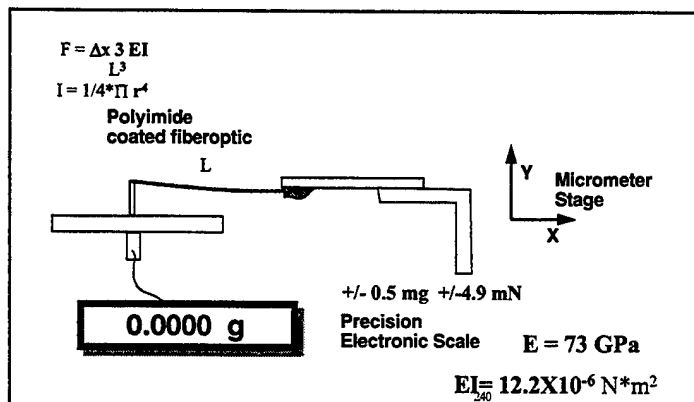
Figure 15 - Graphical description of fiberoptic probe calibration setup

Dynamic Range

The Dynamic range of this system is fixed by the resolution to which one can measure the deflection of the device under test. A typical dynamic range for this method is approximately 2 orders of magnitude. The upper end of the range is limited by the

22

fiberoptic beam tip deflection. The deflection of the end should not exceed 15 % of the length so as to stay in the linear region where the simple beam theory is accurate. In addition, as the fiber is bent passed this point during the application of force to the device it will begin to slip over the part or entirely off the part. When this is encountered the fiberoptic length should be shortened to get a stiffer beam.

Force Measurement Results

What make these devices unique are the high forces with the large deflection. The forces required by the actuator to move a cantilevered 125 micron diameter fiber in a typical hermetic package in which the fiber is cantilevered by 0.5-10 mm is shown in Figure 16 for a deflection of 40 microns. The equation that describes force versus deflection for a cantilevered fiber optic beam can be simply described with the following equation [35]:

$$F = \frac{\delta \cdot 3 \cdot E_S \, I_T}{(L)^3} \cdot 10^6 \quad \text{micro newtons} \tag{1}$$

Where L is the length of the cantilevered fiber optic, δ is the tip deflection in meters, and E_s [73 GPa] and I_T are the modulus of elasticity for fused silica and moment of inertia for the fiber optic, respectively. As can be seen from Figure 16 a 2 mm cantilevered fiber with a deflection of 40 microns has a total restoring force of ~13 mN. The bending of the fiber optic and counter force springs are by far the most significant forces which have to be overcome by the actuator. In addition, the actuators will have to overcome the forces associated with wirebonds and stiction/friction to align the fiber with its coupled device, and hold it in place during subsequent bonding.
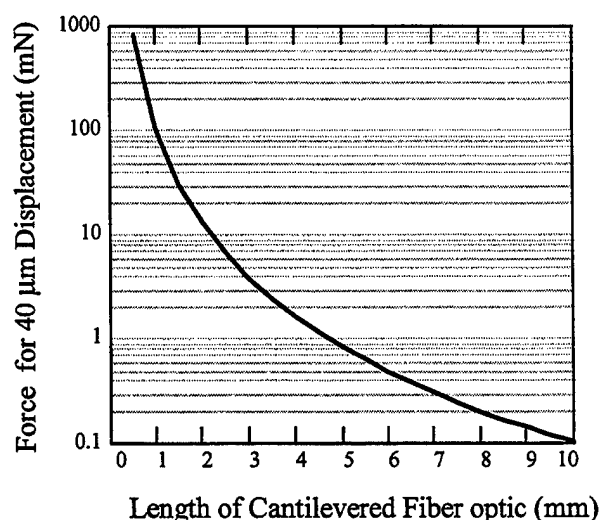
Figure 16 - Restoring force for a 125 micron fiber optic displaced 40 microns versus cantilevered distance

The measurement of force involves the accurate measurement of the fiber optic force probe base deflection and movement of the springs and actuator to which the fiber optic force probe is being applied.[34] By measuring the fiber optic probe tip deflection the applied force to the actuators is calculated. There is a limit to how much force could be applied to the actuator before buckling occurs. Therefore, a small displacement on the actuator of 5 microns in the direction opposite that of the actuator movement was used to measure the force that an actuator can exert at different power levels. A plot of the force versus poly-heater power curves for the in-plane actuators are shown in Figure 17 and Figure 18. As can be from Figure 17, in which the poly-heater has been thermally relieved by a backside anisotropic etch, the available actuator force increases with power. At the 0.3 watts dissipated on the poly-heater the available force is >12 mN for the 5h design and projected >60 mN for the 10h design. By comparing Figure 17 and Figure 18, the thermally relieved poly-heaters are approximately ten times more efficient then the non-thermally isolated heaters. The counter force springs, which are in compression in Figure 9, were designed to bring the actuator back to the reference position, overcome the forces from the friction and wirebonds, and hold the actuator/fiber assembly in place during handling. The nickel LIGA springs where designed to provide 0.5 mN when deflected by 100 microns using 210 Gpa for the modulus of elasticity of electroplated nickel. The force probe was used to measure this and the results are shown in Figure 19.

* 240 micron Diameter Polyimide Coated fiberoptic
* Fiber optic Length = 11mm
* Forced measured at 5 μm back deflection of actuator at each power level
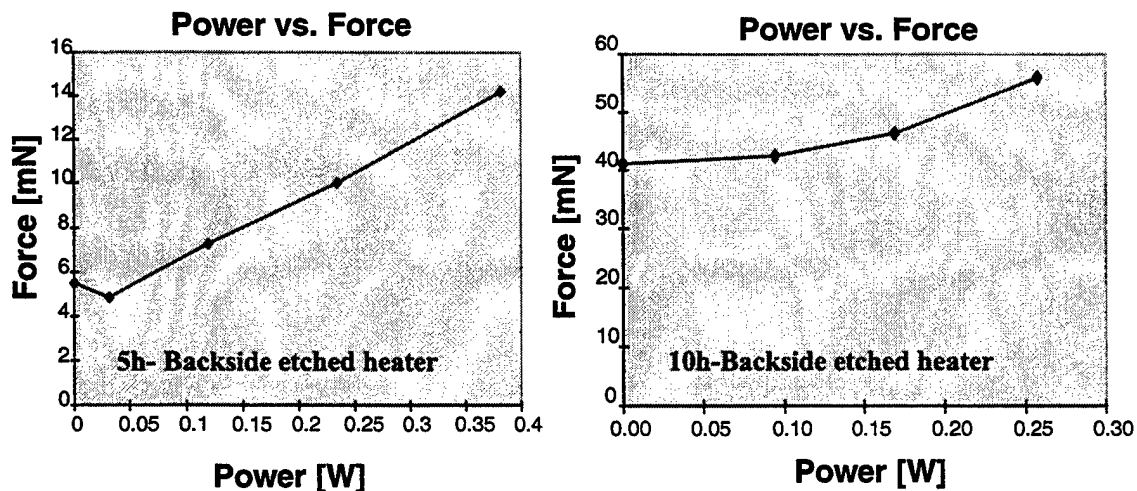
Figure 17 - In-plane thermal actuator force versus power - Backside etched thin-film heater
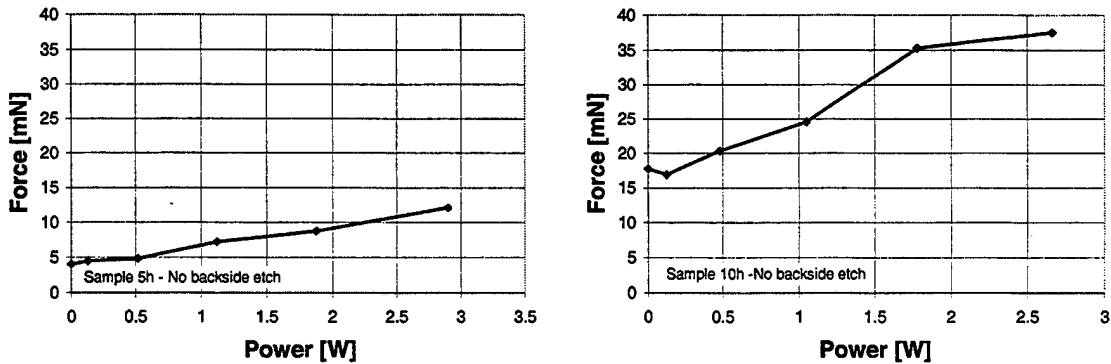
Figure 18 – In-plane thermal actuator force versus power – Non backside etched thin-film-heater
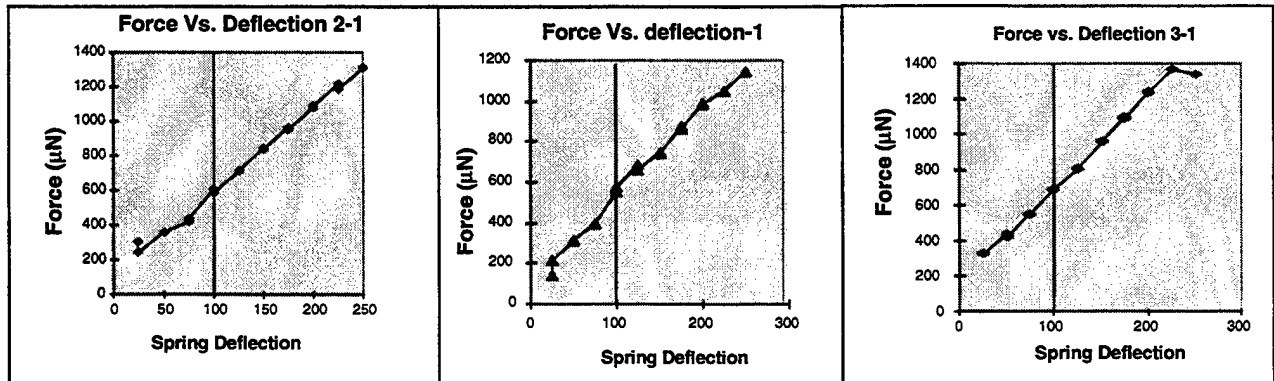
Figure 19 - In-plane counterforce springs restoring force versus displacement – 3 different spring designs

Friction/wirebonds

The stage, which holds the fiber, slides across a substrate. The stiction/friction associated with the manipulation of the actuator across the surface was measured by utilizing the above mentioned fiber optic force probe. The stiction and friction were measured on two surfaces: lapped 6061 aluminum (800 grit) and polished silicon wafer. The mean and standard deviation [σ] results are shown in Table 3.

Device Weight [mg]	Stiction (6061)	Sliding friction (6061)	Stiction (silicon)	Sliding friction (silicon)
295	107 μN σ=11 μN	76 μN σ=11 μN	36 μN σ=5 μN	23 μN σ=3 μN

Table 3 - Measured friction between substrate and IPMA

These empirical results show that stiction and sliding friction are insignificant when compared to the fiber restoring force or the counterforce springs. The force associated with wirebond stiffness can be calculated by using equation 1. The wire bonds are pure

25

gold [E=74GPa] 25 μm by 3 mm long. Assuming 40 μm of deflection the calculated resistance force for four wirebonds is ~ 24 μN. Again much lower than the forces due to the fiber optic and counter force springs.

Dynamic Characterization

Frequency Bandwidth

One of the benefits of the IPMA is it allows continuous actuation. Applications include continuous alignment for plastic packaging and extreme environments, optical switching and phase shifting. For these dynamic applications the frequency bandwidth and fatigue life of the IPMA will have to be understood. A laser vibrometer was used to measure the rate at which an unloaded actuator could move axially. In Figure 20 a plot of the frequency bandwidth shows a -3db point at approximately 60 Hz for two different devices at the same sinusoidal input voltage.

Conditions: A unloaded Design III, [wire bonds and friction]

- 3 dB @ 60 Hz
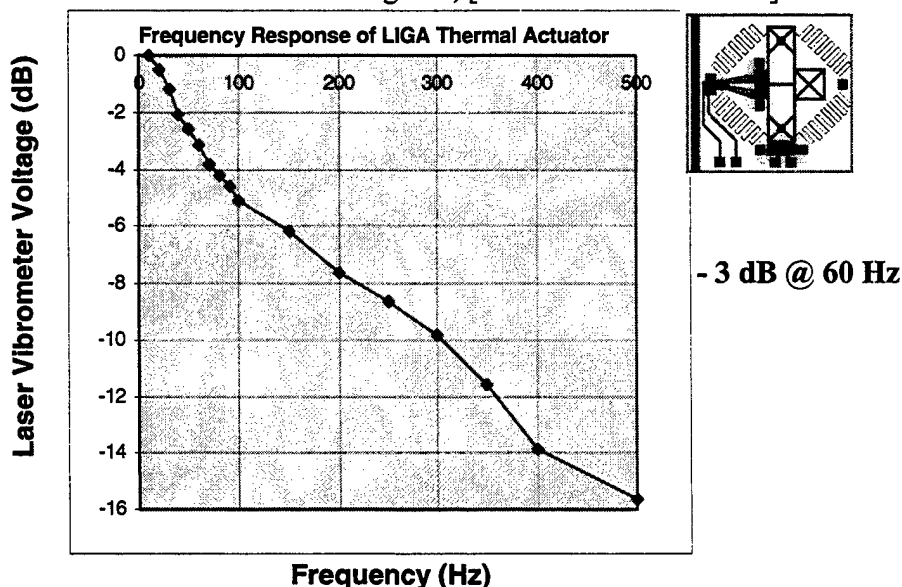
Figure 20 - Mechanical frequency of unloaded in-plane actuator

Life Test

The fatigue life of MEMS actuators was explored. These actuators undergo large displacements upon actuation and therefore there is a potential for metal fatigue. A total of fourteen in plane actuators were characterized for force and displacement. These devices have been put on life test [Figure 21] and cycled for over 10 million cycles at 1 Hz no load. Of these 14 actuators, 3 have undergone deflections >20 μm over the life test without any failures.

26

Two in-plane actuators per device

Started
July 9, 1997
Ended
Nov. 26, 1997

* Test all Devices
Force and Deflection
* To be Retested for
Force and Deflection

Function Generator

HV AMP

Precision Resistor

+ 10 million cycles without
any noticeable degradation

DMM
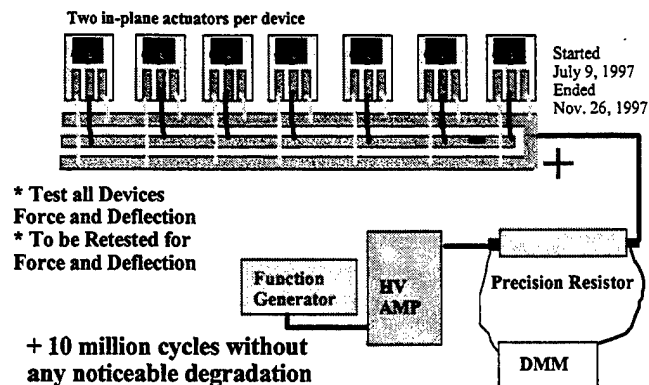
Figure 21 - Fatigue life experimental set-up

Vibration Evaluation

The AMPS aligner was evaluated for its ability to withstand vibration environments. The vibration goals used for this evaluation were conservatively established based on typical, worst case fighter aircraft/missile fuselage environments:

1. All natural frequencies of the aligner should be above 2000 Hz.

2. All actuators should have a force output capable of overcoming a 100 g-peak vibration environment.

The worst case, unmounted design platform mass of 28.1 milligrams was used throughout this evaluation. This results in a minimum stiffness of all return spring and actuators of 4500 N/m and a minimum actuator force output of 28 μN. Table 4 shows a comparison of the significant elements of the AMPS aligner with the vibration design goals.

Element	Frequency	Percent of Goal Frequency	Actuation Force (mN)	Percent of Goal Force	Remarks
In-plane Return Springs	67 Hz	3.4%	N/A	N/A	
In-plane Actuators	2690 Hz	135%	40	143%	10h Backside Etched Actuator
Out-of-plane Actuator	1460 Hz	73%	>500	1800%	Estimated forces

Table 4 -Vibration Evaluation Results

27

Conclusions: Clearly the stiffness of the in-plane return springs needs to be increased significantly. Increasing this stiffness to the same level as the in-plane actuators will provide the desired design margins on frequency and will not significantly degrade the force margin. The in-plane actuator force shown in the table is the minimum value available (at 0 displacement). The force available actually increases with increasing deflection up to over 60 mN. Even if the return spring stiffness is increased to the recommended value, the in-plane actuators will have enough residual force to exceed the actuator force goal by more than 40% at all deflection values. The second conclusion from this evaluation is that the current design for the out-of-plane actuator is larger than it should be. This actuator has very large margins on force and displacement and is marginally low on frequency. Reducing the length of this actuator from 2.7 mm to 1.5 mm will provide a margin of +75% on frequency (>3500 Hz) while maintaining a factor of 3 margin on displacement, and a factor of >3 margin on forces, as well as help reduce the overall size of the device.

ASSEMBLY PROCEDURE

The advantage of using the IPMA is that hybrid components that were designed to ~1 μm tolerance can be designed to within ~10 μm and still be within the 20 μm deflection range.

There are two designs, the mounted and unmounted designs. The mounted design positions the in-plane actuators about the periphery of the fiber-holding movable platform connected to the unmovable portion by springs. The movable portion of the platform also contains the out-of-plane actuator [Figure 10]. This device can be first bonded into a package using standard opto-electronic placement techniques within the actuator range (~10 μm) in front of a laser diode. The laser diode can also be mounted on the non-moving portion of the silicon substrate using passive LIGA stops to preposition the laser in front to the fiber. After the actuator is placed into the package, the lensed fiber optic or other optical component can be brought in and bonded into the fiber holding structure. After the fiber optic is bonded, the actuator can be actuated to align the fiber to the laser diode.

The unmounted device requires a micromachined alignment cavity but is smaller due to the fact that all the actuators are on the same silicon movable base [Figure 9]. The lensed fiber optic or optical component can be bonded to the silicon base at a separate fabrication station. This system would then be placed into precision alignment cavity in front of the opto-electronic device. If such a device is a high power laser requiring a copper heatsink, the alignment cavity can be made using the same LIGA technology used to make the Nickel springs and actuators. If low expansion ceramic material is required, a LIGA mold can be made to make a slip cast ceramic alignment cavity [20]. After the fiber optic/actuator is placed in the alignment cavity it can be actuated to align the fiber to the laser diode.

IN PACKAGE DEMONSTRATION

An IPMA device will be mounted in a Boeing standard Kovar hermetic package. A 911-nm index guided laser diode will be used as the source to which an unlensed fiber will be aligned. The power to the actuators will be supplied via the extra pins available on a typical 14-pin butterfly package. See Figure 22. After the components are propositioned into the package, an initial alignment test will be made and the package will be sealed using Au/Sn [280C] solder. The Fiber optic feedthrough will be sealed with epoxy. Inside the sealed packages the IPMA will be align the fiber optic to the laser diode. Sinusoidal signals will be applied to each actuator as shown in Figure 23, and the coupled power level will be measured. This will demonstrate the ability to perform in-package actuation of a fiber optic.
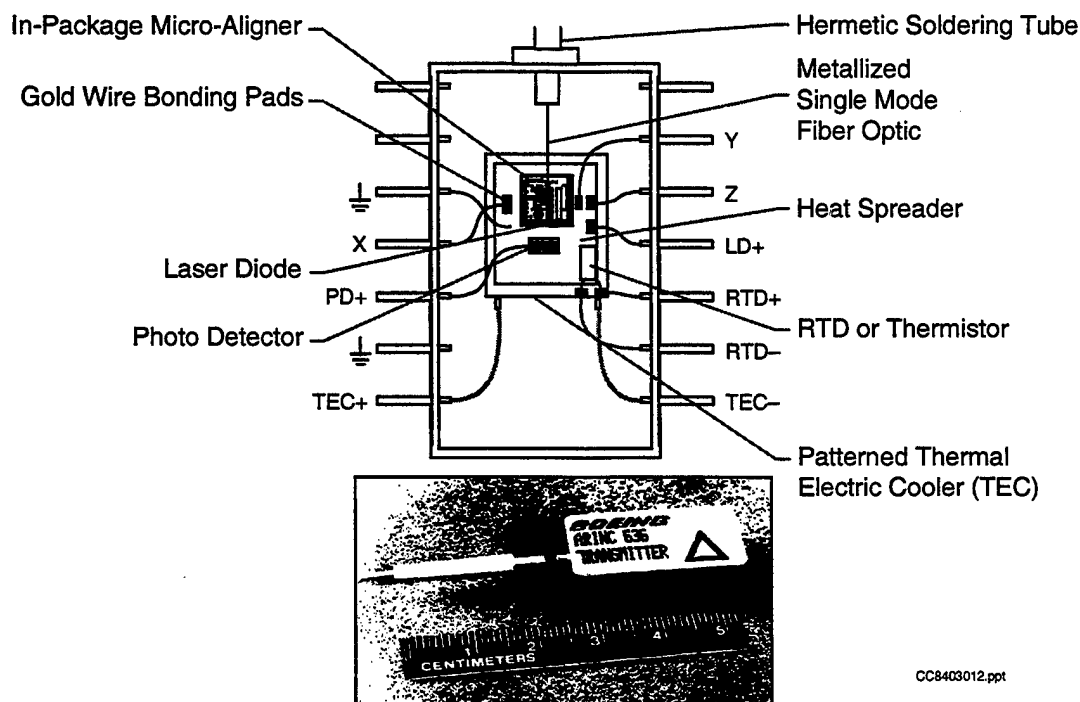
Figure 22 - In-package micro aligner shown to scale in Boeing transmitter package
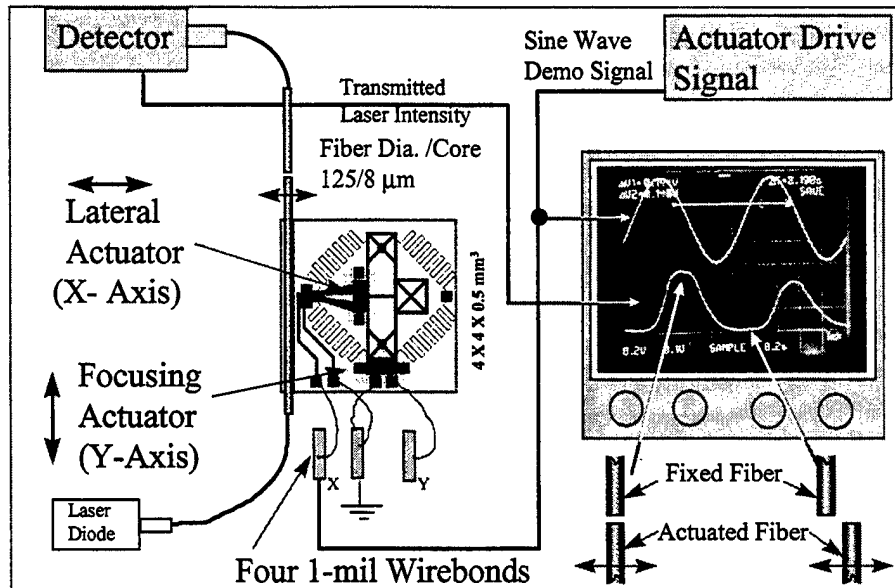
Figure 23 - Two-Axis active fiber aligner experimental set-up and demonstration

Several issues still need resolution for the use of the self-contained IPMA in the single-mode opto-electronic manufacturing environment. Chief among these is the requirement to bond the fiber while maintaining alignment. Thermo-mechanical effects must be dealt with at the package level to avoid unacceptable loss of alignment during bonding. Several bonding strategies are being considered to mitigate this effect. The advantage of having the IPMA and heaters to melt solder in the package is that multiple realignment can be performed without tying up the manufacturing process flow. Laser welding or capacitive discharge welding of LIGA parts will eventually be the bonding processes of choice. Since the fiber is intimately bonded to the stage, this extra mass is a benefit to laser welding or capacitive discharge welding in that this systems has more mass to resist movement than a bare fiber.

LIGA CONCLUSIONS

The IPMA is a tool that gives the EO packaging industry new and untapped freedoms. The IPMA potentially eliminates the need for expensive external automated fiber alignment systems. The current automated external alignment systems are package and device specific. Like any tooling, it requires different fixtures and tooling to hold packaging and to position and bond the coupled fiber. Economics is the final arbitrator. Currently every device and package change requires a costly manufacturing tooling change. This economic rule applies across the photonic product development history; research experimental setups, laboratory prototype production, manufacturing prototype production, and full production. Each one of these stages requires more investment in fixturing and tooling.

The advantage of the IPMA is that the device is so small that it will fit inside the package, removing the need for the tooling and package specific external alignment

systems. The current designs have yield forces and displacement several times larger than required. The current size of the prototype is about three as big as it needs to be and future designs can easily be smaller than 1 mm^2 enabling multiple-fiber attach to a single photonic device. Current and future devices can fit into virtually any current package or experimental set-up. Some packages could be further reduced in size due to the fact that there will no longer be a requirement to fit external effectors to grab fiber optics and micro-optics in the package. For low capitalized companies and individuals the IPMA is a totally new tool that eliminates the need to do manual alignment requiring tens of thousands of dollars worth of manipulating stages and therefore enables them to do cost effective experimentation and prototyping.

In the high volume-manufacturing environment, the choke point is the fiber optic alignment. To get many fibers aligned many machines have to be purchased. This choke point is eliminated by the IPMA, which places the 3-axis fiber optic pigtailing robot into the package. Using a simple desktop computer and array of detectors, many simultaneous alignments can be realized. This alone will significantly reduce the cost of all fiber optically pigtailed components.

PZT BASED PROCESSING FOR AN IN PACKAGE ACTIVE MICRO ALIGNER

PZT Materials For AMPS

The objectives of this program were to establish lead zirconate titanate (PZT) processing infrastructure to support processing of 4-inch wafers with PZT integrated with MEMS structures, and to fabricate simple diaphragm and cantilever structures as a demonstration of the process and functionality of the PZT material. The initial focus was in procurement of equipment for PZT sol-gel processing to permit cleanroom-compatible fabrication of PZT MEMS devices. Major procurements included: a glovebox for formulation of the sol-gel precursor, a spin coater with hotplate for applying the sol-gel to 4-inch silicon substrates, and modifications of an existing annealing furnace to achieve the desired crystallographic orientation. Equipment was purchased and installed during the first quarter of the program.

Sol-Gel PZT Deposition
Sol-gel synthetic routes were adapted from work performed at Sandia National Laboratory and Penn State University. The basic process consists of formulating the sol-gel precursor materials, spin coating on a metallized silicon substrate, baking, coating more layers iteratively until the desired film thickness is achieved, then annealing to convert the PZT to the perovskite crystallographic orientation (Figure 24). Synthesis of $Pb_{1.05}(Zr_{0.53}Ti_{0.47})O_3$ was performed according to the inverted mixing order (IMO) procedure and was deposited on several different substrates including platinized silicon wafers, platinized silicon dioxide coated wafers, and platinized low stress silicon nitride coated silicon wafers. Deposition consists of 500 rpm dynamic dispense for 20 sec.

followed by a 3000 rpm spin for 40 sec. A post-spin bake of between 300 - 350°C is done after each deposition to pyrolyze the film to an amorphous microstructure. The high temperature anneal consists of a ramp to 550°C with a 15 minute hold followed by a ramp to 675°C for a 30 minute anneal, followed by a cool down to 75°C.
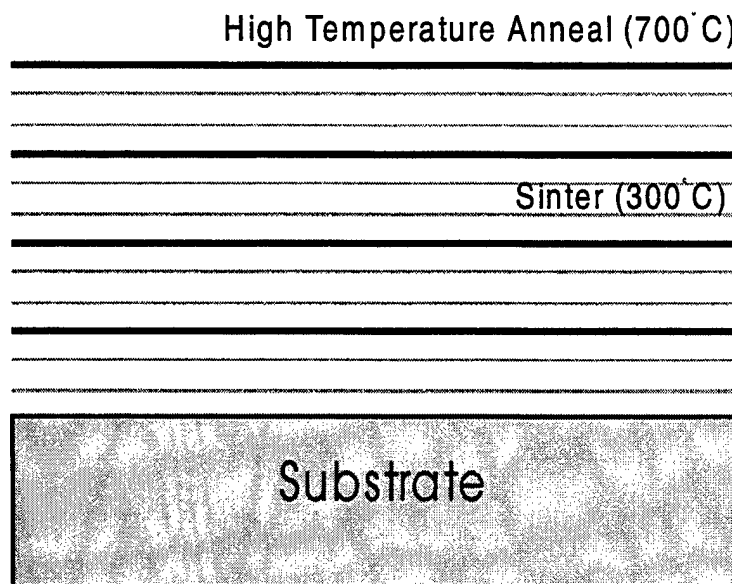
Figure 24 - Basic process for sol-gel deposition of PZT

It was determined that no more than four layers (approx. 400 nm) can be deposited without cracking. However, by annealing after the first two layers, films up to 10 layers (this is not the limit, but simply the maximum that has been performed) can be deposited with no signs of cracking. Presumably, the initial annealing step results in a PZT layer in the proper crystallographic orientation which then acts as a subsequent "seed layer" for further deposition.

Films were analyzed to determine the electrical and morphological properties of the PZT. Ferroelectric and x-ray diffraction testing of 0.5μm PZT films on platinized silicon nitride was performed by Argonne National Laboratory. The same material was imaged with the SEM and Auger spectrometer at MCNC to determine the morphological and chemical properties of the film. Results of these analyses are summarized in Table 5. It is evident from these data that the desired Perovskite phase is the predominant crystallographic form of the PZT deposited in this manner and piezoelectric properties suitable for a MEMS actuator.

Sample	PZT [001]:PZT [110]:PZT [111]	Normalized [110] Ratio	Normalized [111] Ratio	Comments
700C, 60 sec	180:40:40	4.5:1:1	4.5:1:1	small pyrochlore peak, predominant [001]
700C, 120 sec	170:50:50	3.4:1:1	3.4:1:1	peak at 33.5 deg??
725C, 60 sec	170:25:150	6.8:1:6.0	1.1:0.2:1	pyrochlore, [001] nearly equal to [111]
725C, 90 sec	160:15:40	10.7:1:2.7	4.0:0.4:1	dominant [001], little pyrochlore
725C, 120 sec	150:10:50	15.0:1:5.0	3.0:0.2:1	good
750C, 45 sec	240:75:125	3.2:1:1.7	1.9:0.6:1	strong [110] and [111] peaks
750C, 60 sec	160:75:60	2.1:1:0.8	2.7:1.3:1	smaller [001] : [110] ratio

Table 5 - Morphological and chemical properties of sol-gel film

Annealing the PZT layers using a rapid thermal anneal (RTA) process rather than a furnace was also investigated. It was determined that RTA annealing at 725C for 90 - 120 sec. in an oxygen ambient resulted in the best PZT materials. Perovskite PZT was confirmed with XRD data from Argonne. It was found that this produced predominantly [001] oriented material, with little pyrochlore. Lower annealing temperatures (650 and 700oC) had pyrochlore present, while the higher temperature (750C) resulted in [110] and [111] peaks which are not desired for the maximum d33. Ferroelectric test data indicated leaky loops for all samples, but the best materials were RTA'd at 725C as the XRD confirmed. Also it was determined that the RTA process gave much lower defect density than furnace annealing. Moreover, RTA provides much greater throughput and cleanroom process compatibility than furnace processing. Thus RTA annealing of PZT is viewed as a significant breakthrough in establishing a MEMS-compatible process.

PZT Process Integration

Integrating the PZT deposition process with cleanroom MEMS fabrication required addressing several process issues (Figure 25). The first is the need to pattern the PZT layer lithographically, using an organic resist. Dry etching was ruled out due to previous reports that this is a very slow etch process which results in difficult etch residues. Wet etching was used instead, and an etch chemistry based on hydrofluoric acid was found to provide acceptable results. Wet etching produces undercutting which limits the smallest PZT structure to about 5μm in width. Since most "real" MEMS applications of PZT as an actuating member would be larger than this by a factor of ten, the undercut effect is not an issue.
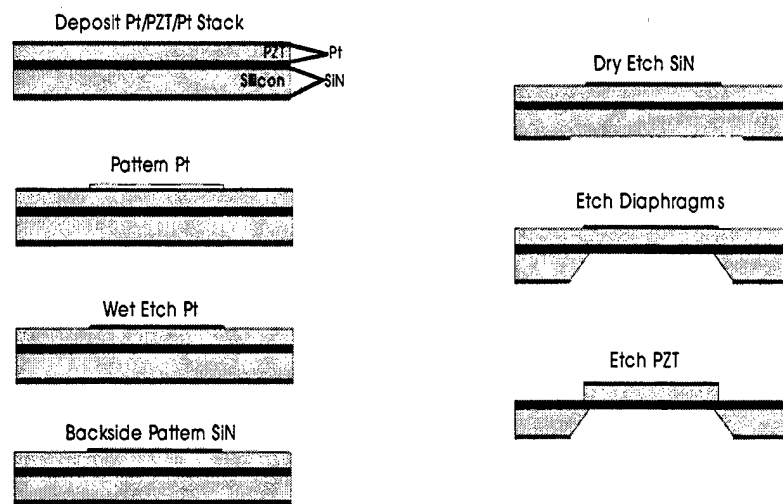
Figure 25 – Basic MEMS fabrications process to form PZT diaphragms

Another process integration issue concerns patterning of the PZT electrode layers. Metal layers above and below the PZT layer are required for actuation, and these layers must be terminated at electrically isolated bonding pads for external connection. At the outset of the program it was assumed that only platinum deposited via high temperature ion-beam evaporation would be acceptable as a bottom electrode. This is because all previous published reports indicate that the morphological form of this platinum layer is critical in orienting the PZT layer in the Perovskite phase.

This creates a process dilemma in that platinum is very difficult to pattern subtractively, i.e. by etching a blanket layer through a mask. The more conventional approach is to additively pattern the metal via a lift-off technique. The high temperature of the ion-beam deposition prevents straightforward lift-off processing, however. Conventional e-beam evaporated platinum as well as other more easily patterned metals were thus investigated as possible electrode materials for PZT, as discussed below.

A third process integration issue involves masking of the PZT from silicon bulk etching required to form the MEMS mechanical structure. Conventional processing relies on potassium hydroxide based anisotropic (crystallographic) etching to form these silicon structures. PZT is chemically attacked by this etch and therefore must be masked. Frontside protection schemes used for protecting aluminum in other MEMS designs were adapted for use in forming PZT diaphragms, with partial success.

Diaphragm and cantilever test structures were designed to assess PZT piezo-mechanical properties. These structures were designed to provide characterization of PZT for out-of-plane actuation in AMPS devices and to integrate the PZT deposition process with the cleanroom MEMS process for the first time. Process issues associated with this integration prevented completion of functional devices. The biggest problem was preventing attack of the PZT layer and associated electrode metallurgy during bulk

34

etching of the silicon wafer. Bulk etching is required to form the diaphragm or cantilever.

The best protection scheme tried was a combination of frontside coating with a spin-on polymer film along with fixturing the wafer so that the frontside of the wafer is not exposed to the etchant. This performed adequately for diaphragm etching, but is not suited to cantilevers due to the fact that cantilever etching provides a pathway through the wafer allowing attack of the frontside. Better frontside protection schemes are required to prevent this attack. Alternatively, deep reactive ion etching (DRIE) may prove useful in bulk etching silicon for PZT actuators. Tooling for this process has recently been installed in MCNC's cleanroom and has demonstrated ability to do through-wafer etching such as that need for definition of cantilevers.

PZT Electrode Materials

As previously mentioned, platinum is the most commonly used metal for defining PZT electrodes. Depositing platinum on a MEMS type substrate such as a silicon nitride layer requires the use of an adhesion layer between the platinum and the nitride. In processing the PZT through MEMS fabrication it was noted that adhesion loss occurred at the platinum/titanium interface. This loss occurred during stripping of the photoresist layer used to protect the PZT during anisotropic etching. X-ray photoelectron spectroscopy (XPS) showed no evidence of contamination at the interface, but did reveal that the titanium was present as titanium dioxide rather than as the original metal. This indicated that oxygen had diffused through the platinum layer. As TiO_2, this layer is no longer adherent to the platinum. Intentionally converting the Ti layer to oxide followed by platinum and PZT deposition verified that TiO_2 is not sufficiently adherent.

Chrome was investigated as an alternative since this metal is commonly used in MEMS as an adhesion layer. However, in the PZT process it was found to delaminate after only $0.2\mu m$ (two layers) during the RTA cycle. XPS analysis of the pre-and post-RTA samples showed that, at 725C, Cr readily diffused through the Pt and PZT layers and ends up on the surface.

Other PZT researchers have noted that Tantalum works well as a Pt adhesion layer and also survives further processing. Deposition of $0.8\mu m$ of PZT on Pt/Ta films using a three-layer RTA anneal process showed that the Ta/Pt layer does indeed maintain good adhesion, especially when preceded by an oxygen plasma preclean. With good adhesion characteristics and inertness to other process steps, tantalum was selected as the best adhesion layer for Pt/PZT.

PZT TESTING PROCEDURES AND RESULTS

Structural and Electrical Characterization of PZT Films Synthesized by Sol-Gel at MCNC

Films were synthesized at MCNC and characterized at ANL, using X - ray diffraction, Rutherford Backscattering spectrometry (RBS), and electrical measurements to characterize the structure (i.e., film orientation of the ferroelectric layer), composition, and polarization characteristics of $Pb(Zr_{0.53}Ti_{0.47})O_3$ (PZT)-based capacitor structures, which are similar to the electrode/ferroelectric/electrode structures needed for MEMS actuators. The X-ray diffraction and RBS analysis, and the electrical measurements were performed using the X-ray diffractometer, RBS accelerator, and dedicated RT 6000 - Radiant Technology electrical characterization systems available to the Interfacial Materials group of the Materials Science Division at ANL. A summary of the main results is presented in Table 6, and a discussion of the main results is presented below.

Synthesis Methods	Electrodes	Substrate	Microstructure	Electrical Properties	Mechanical Properties	Issues
SOL-GEL	PT	(100)Mg)	Highly (001) oriented PZT film	40-50 C/cm	not measured	Needs layer-by-layer spin-on deposition (~900 A each) with a curing step (~300C) and an ' annealing step (~700-725 C) after each spin to avoid film cracking (growth time film (~1 m in 6 hrs).
SOL-GEL	Pt/Ti	(100)Si	Polycrystalline	15-20 C/cm	(~10 m deflection for a 2 cm long beam)	Same Synthesis issues as above. In addition, some films pealed-off. Ti is not a good diffusion barrier. We recently demonstrated by in situation scattering analysis that Ti diffuses into Pt, inducing film pealing due to Ti loss at the Ti/Si interface. We have also shown that Pt/Ti02 is a eastable electrode and would be a solution for PZT integration with Si MEM
SOL-GEL	Pt/Ta	(100)Si	Polycrystalline	15-20 C/cm	not measured	Same synthesis issues as above. We demonstrated synthesis of four spin-on PZT layers with only the curing step (300 C)

						between each layer and 700 C anneal after the fourth layer only. This reduces processing time or 1 m film by ~1 1/2h. No film cracking was observed.
MOCVD	Pt	(100)Si	not measured	not measured	not measured	PZT film grown in vertical MOCVD system to investigate step coverage. Excellent step coverage demonstrated. Advantages of MOCVD: a) Excellent step coverage: b) Fabrication of ferroelectric films as deposited withou post-deposition processing; c) feasibility of growing good lattice matching oxide electrode and ferroelectric layers in an intergrated cycle in the same C system; d) sealing to cover large are substrates; e) control of films orientation and microstructure through synthesis temperature. Dissadvantages of MOCVD: a) More expensive initial capital equipment than for sol-gel. b) Needs accurate control of precursors delivery; this can be easily achieved with new liquid delivery systems already in the market.
SOL-GEL	Pt/Ta	(100)Si	Polycrystalline	15-20 C/cm	not measured	Same synthesis issues as above. We demonstrated synthesis of four spin-on PZT layers with only the curing step (300 C) between each layer and 700 C anneal after the fourth layer only. This reduces processing time or 1 m film by ~ 1 1/2h. No films cracking was observed. Advantages of SOL-GEL: a) Inexpensive and easy Disadvantages of SOL-GEL:

						a) Poor step coverage: b) Easy cracking of films c) Weet Process
MOCVD Pb (Zr0.53Ti0 .47)03	SrRuO3	(001)Mg 0	Epitaxial (001) oriented PZT film	40-55 C/cm2 (single crystal- type square loop)	not measured	High quality 1 m thick PZT film as deposited at 700 C in about 3 h withoug post-deposition processing. SrRuO3 provides better lattice matching to PZT, inducing films with high crystallinity than with Pt electrodes.
MOCVD Pb (Zr0.53Ti0 .47)03	SrRuO3	(100)Si	Highly (001) oriented PZT film	30-40 C/cm2		Same synthesis issues as above. SrRuO3 is a estable electrode for PZT integration with Si.

Table 6 – A summary of PZT testing at Argonne National Labs

a)Sol-gel PZT films were synthesized at MCNC, using the inverted sol-gel solution and deposition processes developed at Sandia National Laboratory and optimized by O. Auciello and colleagues at NCSU. In this method, a sol-gel solution of morphotropic phase boundary $Pb(Zr_{0.53} Ti_{0.47})O_3$ (PZT) composition (this composition was chosen because it generally yields PZT films with the highest saturation and remanent polarization) was prepared, and films were synthesized on $Pt/Ti/SiO_2/Si$ and on $Pt/Ta/SiO_2/Si$ substrates. These metallic heterostructures were chosen because they are being used to fabricate capacitor for ferroelectric memories, which have an structure similar to that needed for MEMS actuators (i.e., a ferroelectric layers sandwiched between top and bottom electrodes needed to apply the voltages required to induce the piezoelectric deformation of the ferroelectric layer and associated actuation). As indicated in Table 6, there are two main problems associated to the Pt/Ti and Pt/Ta electrodes, namely: a) a visual observation indicated that several films pealed-off, and b) the hysteresis loops were rounded indicating substantial leakage currents (in addition, the polarization values were relatively low; about 10-20 $\mu C/cm^2$) (see .Figure 26 - . The loop shown in this figure is characteristic of a film with undesirable leakage current.

). The poor electrical properties of the sol-gel PZT films grown on the Pt/Ti electrodes are largely due to the poor compositional and microstructural characteristics of the PZT layer, which exhibited the presence of a pyrochlore phase together with the ferroelectric perovskite phase (see XRD data in Figure 27).
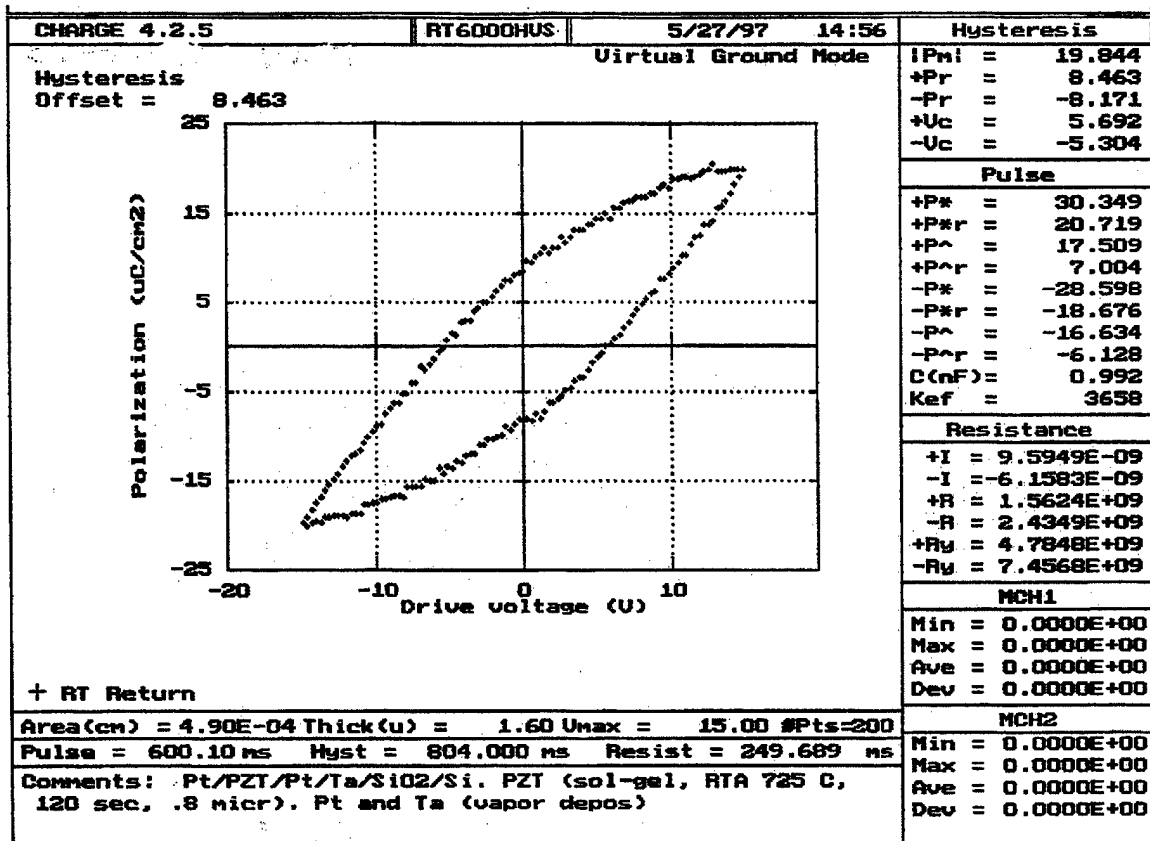
Figure 26 - Polarization hysteresis loop of a $Pb(Zr_{0.53} Ti_{0.47})O_3$ film grown by sol-gel on a Pt/Ti/SiO/Si substrate
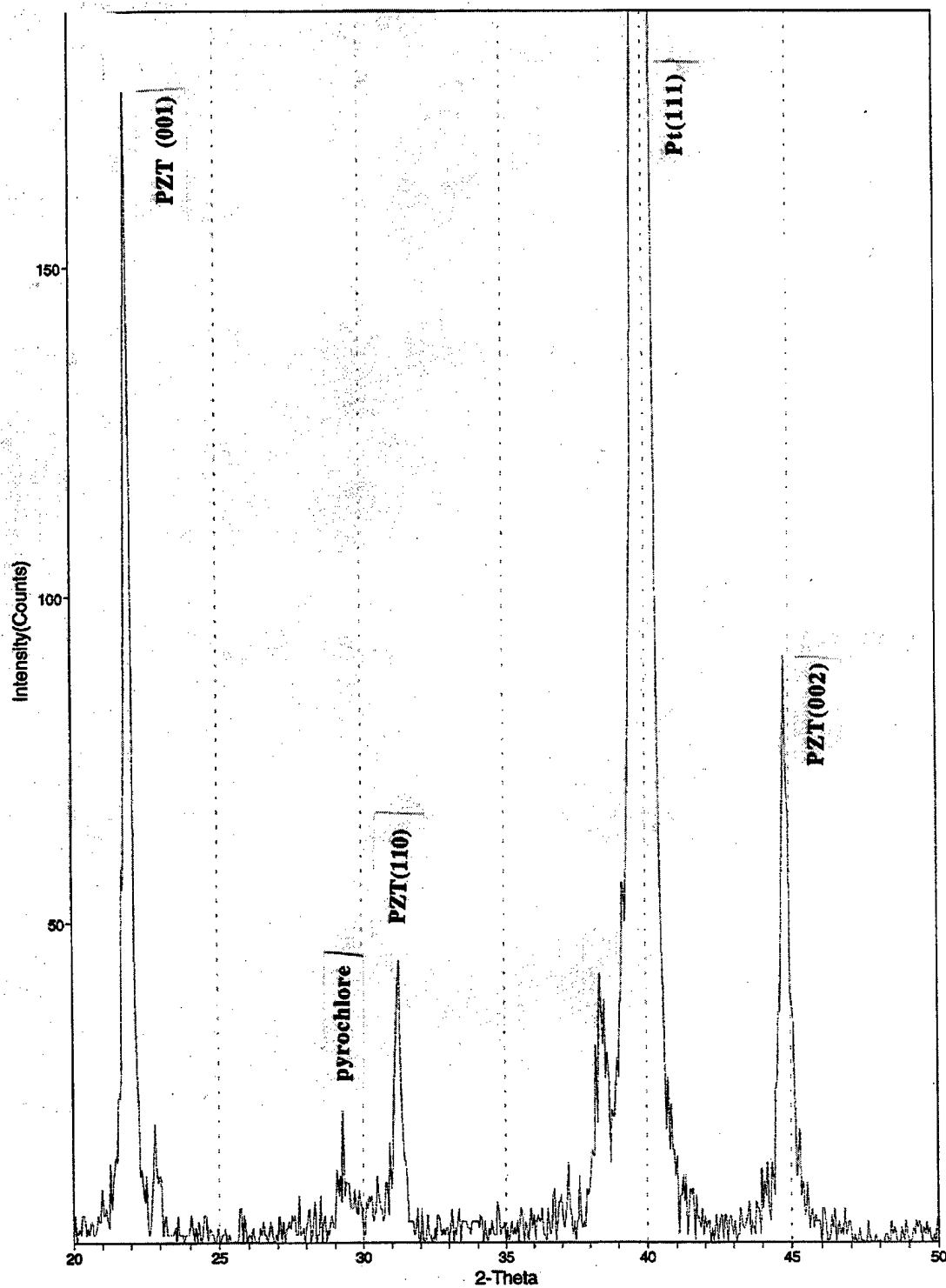
Figure 27 - XRD pattern of the PZT film shown in .Figure 26 showing the presence of an undesirable pyrochlore phase.

b) Although not originally planed, we decided that we needed to understand the reason for the poor performance of the Pt/Ti and Pt/Ta electrode systems, since the bottom electrode determines to a large extent the microstructure and properties of the ferroelectric layer. We used a unique *in situ* time-of-flight ion scattering and direct recoil spectroscopy technique developed at ANL, to investigate the effect of heating, needed to produce ferroelectric films on the Pt/Ti and Pt/Ta electrode systems. We found that heating resulted in the diffusion of Ti or Ta to the surface of Pt. This in turn can affect the stoichiometry of the ferroelectric films. This work indicated that we need to explore alternative electrode materials for integration with or other ferroelectric layers. We therefore explored alternative more stable electrode materials in conjunction with the work focused on the synthesis of PZT by MOCVD.

Characterization of Mechanical Properties of PZT Films Synthesized by Sol-Gel at MCNC

Limited characterization of mechanical properties of PZT films grown on Pt/Ti/Si were performed at Boeing (former McDonnell Douglas). This characterization was performed on rectangular 2 cm x 2 mm beams with a Pt/PZT/Pt heterostructure. Deflection values are shown in Table 6. The sol-gel films which mechanical properties were measured at Boeing were prepared by O. Auciello before moving to ANL. Subsequently, upon moving to ANL, O. Auciello continued directing the synthesis of PZT films, which was carried out by B. Augustin at MCNC, while electrical characterizations were performed by O. Auciello at ANL (see Table 6).

MOCVD Synthesis and Characterization of Films at ANL

Based on the problems observed with the PZT/Pt/Ti/Si heterostructures, we investigated the synthesis of PZT films by MOCVD on conductive RuO_2 electrodes. The advantage of using RuO_2 electrodes is that both the electrode and PZT layers can be grown in the same MOCVD system in an integrated process. In addition, we demonstrated that our MOCVD process is suitable to grow both the RuO_2 and PZT layers at low temperature.

RuO_2 bottom electrodes 150 nm thick were grown on Si substrates at different temperatures to control the layer orientation, which affect the orientation of the PZT layer grown on top. Growth temperatures • 300 • C combined with low growth rates (• 3nm/min) favor growth of (110) oriented RuO_2 films (see Figure 28 (b)). On the other hand, low growth temperatures (• 300 • C) and high deposition rates (• 3nm/min) favor growth of (101) oriented RuO_2 films (see Figure 28 (a)). After deposition of the RuO_2 films, PZT layers were grown *in situ* in the same reactor with the substrate held at 525 • C. Tetraethyl lead, zirconium t-butoxide, and titanium isopropoxide were used as metalorganic precursors. The PZT films grown on the (101) oriented RuO_2 electrode layers are highly (001) oriented (see Figure 28(a)), while the PZT films grown on the (110) RuO_2 layers are more randomly oriented (see Figure 28(b)). The dependence of the PZT layer orientation on the RuO_2 layer orientation can be explained to a certain extent in terms of the unit cell matching between the RuO_2 and the PZT layers. Capacitors were fabricated to

41

test the electrical properties of the PZT/oxide electrode heterostructures. These tests demonstrated that MOCVD-PZT films grown on oxide electrodes with controlled deposition conditions exhibit good hysteresis loops with high polarization (see Figure 29), with the (001) PZT having higher polarization than the randomly oriented PZT.
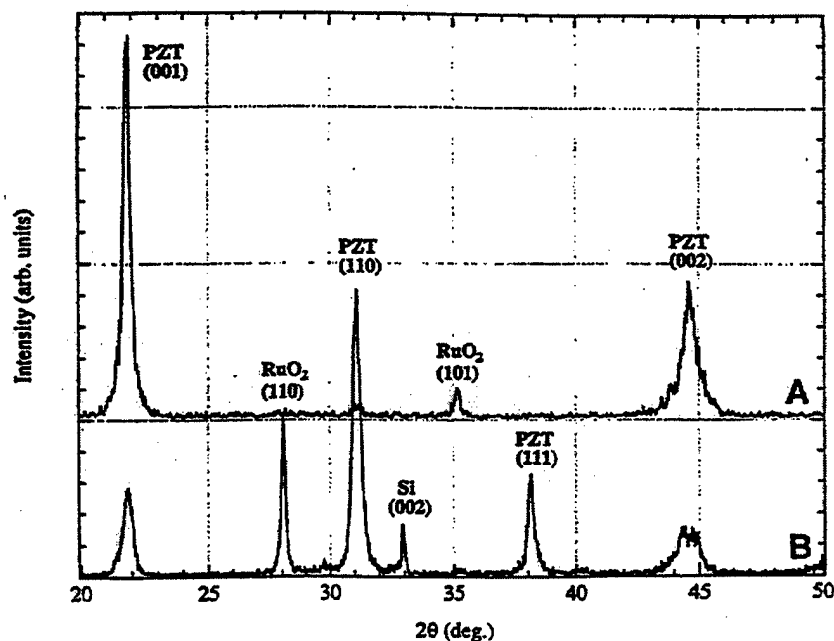

Figure 28 - (a) XRD of a (001) PZT (53/47) layer grown on a (101) RuO_2 electrode. (b) XRD of a randomly oriented PZT (53/47) layer grown on a (110) RuO_2 electrode.
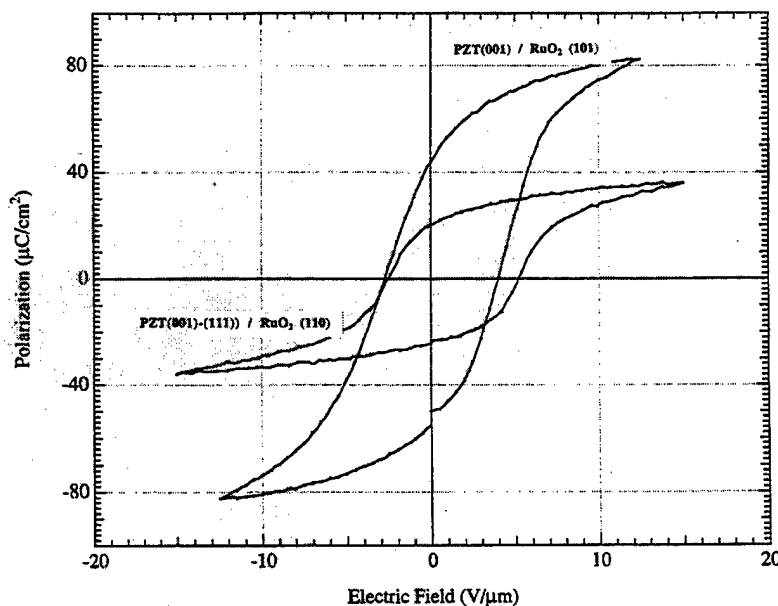

Figure 29 - Polarization hysteresis loops for the (001) and randomly oriented PZT films grown on (101) RuO_2 and (110) RuO_2 electrodes, respectively.

In addition, we also investigated the synthesis of PZT on conductive SrRuO3 electrodes. We have demonstrated that SrRuO3 is an alternative good conductive oxide electrode, which can be grown highly oriented, leading to the growth of highly oriented (001) PZT. Figure 30 shows the hysteresis loop for a SrRuO3/PZT/SrRuO3 heterostructure, which indicate that these films behave like single crystals with an almost perfect square hysteresis loop and close to maximum polarization expected from single crystals. Figure 30 also shows the dependence of the coercive field Ec on the PZT composition. It is expected that the piezoelectric properties of these high quality PZT layers will be excellent. Note that in Figure 30, The films with smaller coercive fields would switch much easier and be most appropriate for low voltage actuators.
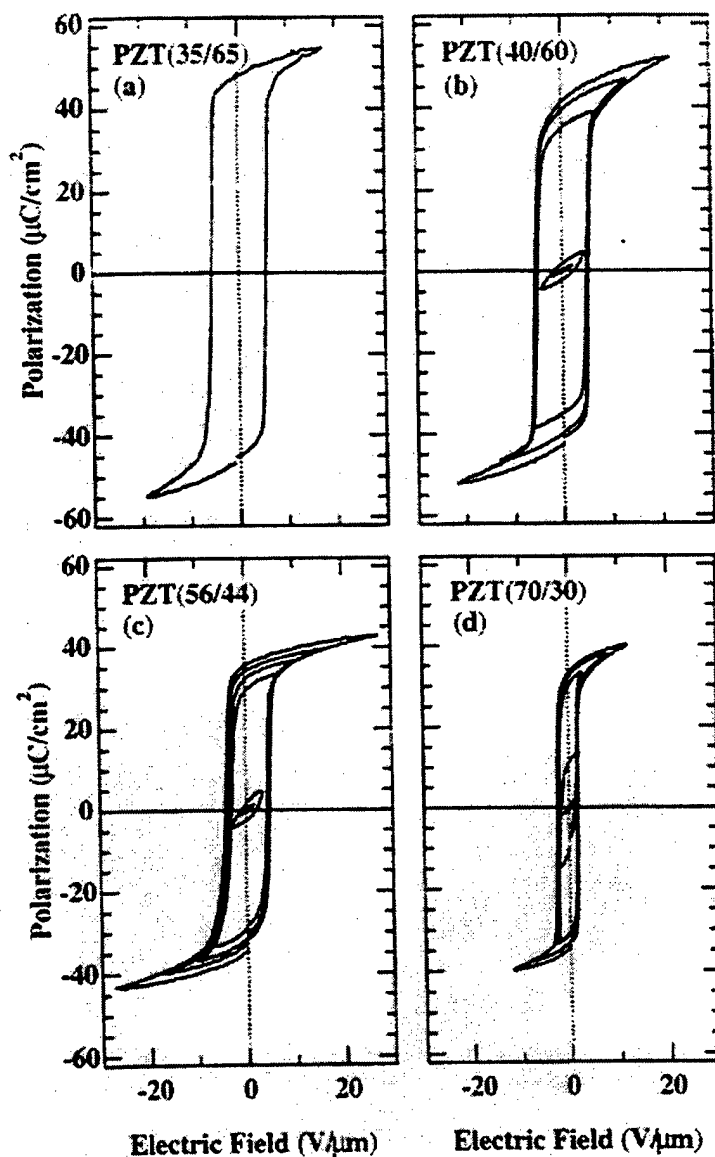

Figure 30 - Polarization hysteresis loops for four PZT films with different Zr/Ti ratio, grown on SrRuO3 electrodes

The initial work on oxide electrode/PZT/oxide electrode structures performed in our laboratory is very promising in that shows that these structures will be suitable for incorporation into MEMS devices including actuators of interest to Boeing.

Assembly of a vertical MOCVD reactor with Large Area Film Growth Capability and Initial Tests

Some of the funds provided by Boeing (former McDonnell Douglas) to ANL, as part of the AMPS program, were used to contribute to assemble a vertical MOCVD reactor with capability to produce ferroelectric thin films on up to 5 " wafers. A substantial part of the funds necessary to assemble the MOCVD reactor was provided by ANL. The system which is now practically completed includes: a) a vertical reactor with a 6" susceptor, which provides the capability to grow films on up to 6" wafers; b) five bubbler- precursor delivery systems; and a commercial liquid delivery system from Advanced Technology Materials. This system will provide the capability for producing ferroelectric films suitable application to MEMS devices of interest to Boeing.

One of the main applications of the vertical reactor MOCVD reactor will be to produce ferroelectric layers with excellent step coverage. As an initial test of the vertical reactor capabilities, we deposited PZT layers on Si samples with various steps defined by lithographic processing. Figure 31 shows the excellent step coverage capability of the vertical reactor. This will be critical for the fabrication of MEMS actuators with movement parallel to the substrate surface.
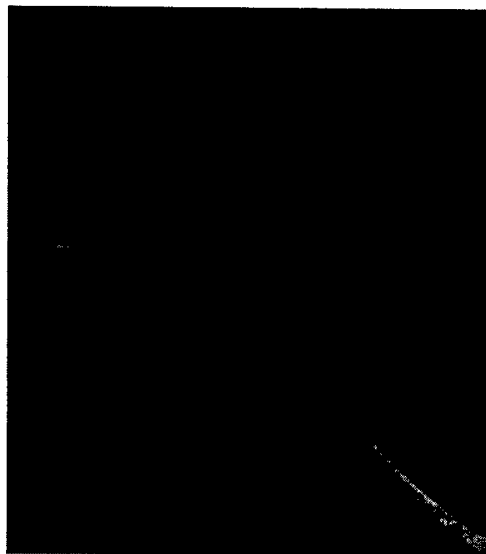

Figure 31 - SEM micrograph of a PZT layer grown on a patterned Si substrate, using the MOCVD vertical reactor

PZT Testing Conclusions

In conclusion, the short research and development program funded by Boeing (former McDonnell Douglas) at ANL provided the basis for producing high quality ferroelectric films and heterostructures with microstructure and properties suitable for application to MEMS devices of interest to Boeing. It is the intention of ANL to pursue further work in the general area of ferroelectric thin films suitable for application to MEM systems and to explore further collaboration with Boeing.

PZT Summary

Work done under the AMPS program has resulted in advancing the state of sol-gel PZT to real-world wafer sizes and with important gains in the understanding of process integration issues. PZT synthesized according to the inverted mixing order (IMO) procedure was found to provide high quality Perovskite films up to $1\mu m$ in thickness. A rapid thermal annealing (RTA) process was developed to improve throughput of the PZT annealing process and to achieve a standard of productivity and defect density necessary for manufacturing in a MEMS facility. Electrode metals have been identified which are compatible with lithographic patterning and which also provide necessary adhesion without compromising the PZT properties. PZT films processed according to these new procedures demonstrate a high content of piezoelectrically active 100 Perovskite phase.

Realizing functional MEMS structures with this material will require additional process development. Specifically, better protection schemes are required to improve the integrity of the PZT through the bulk silicon etch process. This will be particularly challenging for definition of out-of-plane actuators based on PZT-silicon bimorph structures, which are the most straightforward and promising of the PZT MEMS approaches. Application of DRIE may provide the best solution to this problem. This process also presents the opportunity to fabricate in-plane actuators by coupling DRIE with CVD deposited PZT. Initial work at Argonne looks encouraging in this regard.

MEMS applications of PZT, especially for microactuators, will be determined by how effectively piezo actuation properties of PZT competes with other means of MEMS actuation such as electrothermal, electrostatic, and electromagnetic in technical and economic terms. These later approaches are more advanced in their development and number of applications already explored. Applications which require high speed or work/volume may be the main drivers for continuing evolution of PZT in MEMS. Meanwhile, PZT will remain the material of choice for piezoelectric sensing, and the improved sol-gel application will greatly facilitate PZT sensing in silicon-based MEMS.

Finite Element Design Tool Development

FEM Goals

Finite element methods have become a widely used analysis method for a broad range of problem types. Although born out of the solid mechanics area, they quickly found utility in fluid flow, heat transfer, electric field, magnetic field, and other problems. The goal in this development was to create a code that would address the fully coupled problem of a piezoelectric material with thermal effects. Other analysis codes could address various aspects of the problem, however, they did not allow all parts of the response to be included at the same time. Another goal was to have a program that would run on a PC, unlike some of the commercially available codes that require a much larger platform.

Given that there are a number of core functions in finite element analysis that are fundamentally the same, it was decided to take advantage of previous development work as much as possible. All finite element codes result in a system of equations that need to be solved, all have nodes, elements, loads, and boundary conditions that need to be defined for a particular problem at hand, and all require the assemblage of individual element stiffness matrices into the total system stiffness array. It was planned to use the basic logic, at least, from other codes that were developed as a starting point for this new, coupled code.

It was also desired to develop the code in an incremental fashion such that the new code could be compared with some of the other analysis methods whenever possible to ensure the correctness of the solution. To this end, the piezoelectric degrees of freedom were added to the basic solid mechanics code first. This did not include the thermal degrees of freedom, but allowed for the comparison of AMPS results to the ABAQUS piezoelectric element. A separate thermal stress code was then developed which allowed for both static and transient solutions. This was also verified separately. In a final step the two were brought together into the code that is referred to as Coupled Thermal Electrical Mechanical Analysis (CTEMAN for short).

Features of the code

There are four basic element types in the code. All are 8-noded solid (brick) elements, however, they each have a different number of degrees of freedom available to allow the user to address different problems. The formulation and solution of each of these is somewhat different and presented different issues to the development.

First, and perhaps simplest, is just a mechanical response problem. The elements allow linear displacement response (constant strain) and can have either static or transient loads. Transient loads can be represented either by a series of linear segments in time, or a summation of a sine and cosine function. The dynamic response is computed at specific time increments and output is available at all time steps or at some prescribed interval to reduce the volume of output. In addition, displacements can be obtained at

46

specific nodes, and stresses at specific elements. This also helps reduce the output when the user is only interested in the response at specific locations in the model.

Concentrated forces, distributed surface pressures, and specified displacements can be imposed on the model. Constraints can be made in the global coordinate system, or in a direction specific to the node. This allows skewed constraints to be applied to the model.

Piezoelectric analysis is the second type of problem that can be addressed. In this case the electrical degrees of freedom are coupled with the displacements. No thermal capability is allowed. In addition to the displacement conditions mentioned above, voltages can be specified at nodes and electric charge boundaries can be specified. The piezoelectric response is steady state, however, if the displacements are constrained, a transient electric field analysis can be performed.

Both the mechanical response and piezoelectric problems result in symmetric matrices. In these cases only the upper triangle needs to be retained, and a "skyline" procedure is used to prevent the storage of unneeded zeros. A solution procedure that operates on a skyline matrix is included. This results in a very efficient storage and solution process for these cases.

A word about integration schemes seems appropriate at this point. The degrees of freedom associated with the electrical field and the temperature field have no mass. This presents a bit of a snag to the integration process. In the displacement case, Newmark's method is used which is required to deal with the acceleration terms and which takes advantage of the bandedness of the problem. The band characteristics are based upon the node numbering and the fact that in the development of the equations, all degrees of freedom associated with each node are grouped together. Massless degrees of freedom can only be handled in the Newmark method through a partitioning process that would group all the massless dof together. Doing so would, however, destroy the bandedness of the matrix upon which the basic fabric of the code is based. To avoid this problem, a Crank-Nicolson method was used to integrate the equations in the cases of both the transient electric field analysis and the thermal field analysis. Although this works fine in these two cases, it prevents the transient solution from being extended to the completely coupled case. To incorporate transient analysis for the fully coupled case would require that the code be rewritten to allow the type of partitioning needed to isolate the massless dof.

Thermal stress analysis can be performed. The thermal stress response is static, however, a heat conduction analysis (with no displacement degrees of freedom) can be performed that is transient. Nodal temperatures can be specified, as well as convection and heat flux boundaries.

The thermal case results in coupling that is not symmetric. The "skyline" process cannot be used therefore another approach had to be taken to minimize the storage requirements. Depending upon the numbering of the model, either a banded matrix storage scheme is used or the entire matrix must be stored. The tradeoff between these two is discussed later.

Fully coupled analysis is, of course, the ultimate goal. This type of analysis is available in the steady state mode only, as mentioned above. Any combination of "loads" and boundary conditions can be used to assess the effects of the complete coupling. It should be noted that the accuracy depends upon an accurate description of the coupling coefficients in the material matrix. These coefficients may be difficult to determine in some cases.

The program allows linear spring elements (either translational or rotational) to couple any dof to ground. This is useful in obtaining force output for the case of actuators. Various ranges of spring stiffness can be used to determine the force-displacement behavior of the actuator. Care must be taken in interpreting the results to ensure that stability, or other failure criterion, are not exceeded. The program is only linear and does not account for any buckling, nonlinear response, or other failure criterion.

The code was developed in Microsoft FORTRAN. This compiler allows the use of an allocatable memory scheme resulting in a fairly small executable while still being able to address a large problem size. The storage for the stiffness, mass, and damping matrices (and a number of other vectors and arrays) are allocated from the heap at run time when the required size is known. The maximum problem size is only limited by the amount of disk space that is available for virtual memory.

The amount of storage required by the program depends upon the type of analysis that is being used and upon the characteristics of the mesh used to analyze the problem. In the worse case of a fully coupled analysis, the resulting damping matrix is not symmetric. This is due to the coupling between the thermal dof and the rate of change of the electrical and displacement dofs. Even if the matrix is unsymmetric, a particular problem mesh may result in a high degree of bandedness, which still presents some storage improvements if it can be taken advantage of. The program is designed to evaluate the status of the equations and determine the most efficient form for storage and processing of the equations. A symmetric case will be stored using the "skyline" method and a solution procedure is available that takes advantage of this storage scheme. In the unsymmetric cases, the code evaluates the tradeoff between banded storage and just storing the entire stiffness, mass, and damping arrays. Although banded storage may seem to always be an advantage, the solution procedure is different and requires an additional block of memory to execute its algorithm. If the matrix band size gets too large, the combination of matrix storage and solution space can exceed the size needed to store the entire matrix. The complete matrix can be solved in-place eliminating the extra space for the solution algorithm.

Demonstration of Program Features and Performance

To illustrate the capabilities of the code and the performance of the code on the PC, several sample cases are presented. The first is a simple piezoelectric bimorph cantilever beam shown in Figure 32.
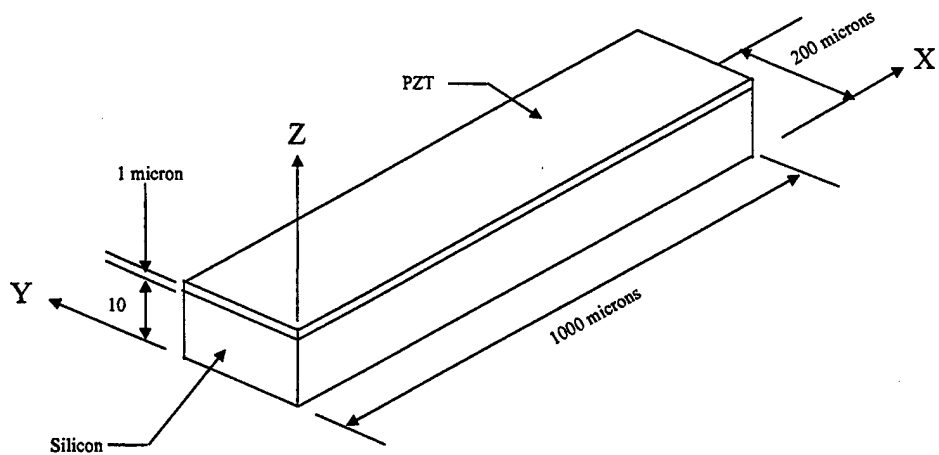
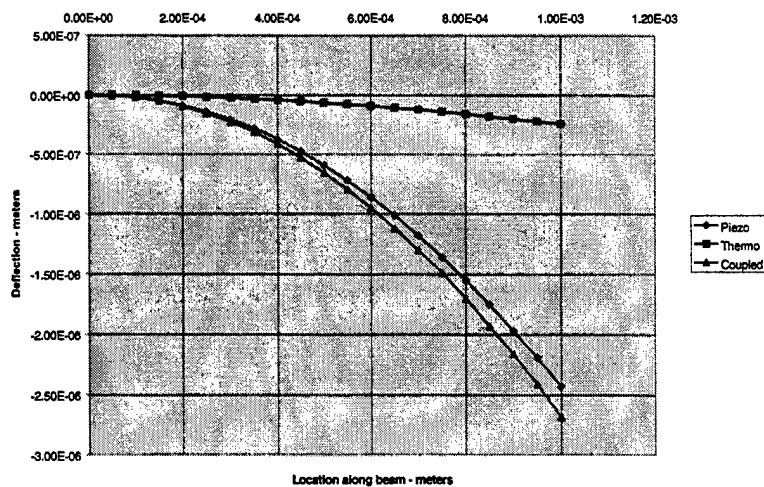**Figure 32 - Cantilever Bimorph Beam**

Figure 33 - Comparison of Thermal and Piezoelectric Deflection

As can be seen in Figure 32, the beam consists of 10 microns of silicon with 1 micron of PZT on one side. A voltage is applied over the PZT and the deflection of the free end is determined. Several aspects of the behavior are illustrated in the following figures. Figure 33 shows a comparison of the deflection along the beam from a temperature change to that obtained with a voltage across the PZT and to the coupled behavior.

Looking more closely at some of the subtler effects in Figure 34, the difference that the pyroelectric coefficients have on the results. The pyroelectric coefficients couple the thermal and electrical degrees of freedom. The effect is, in most cases fairly small, however it is important to get a complete picture of the response.
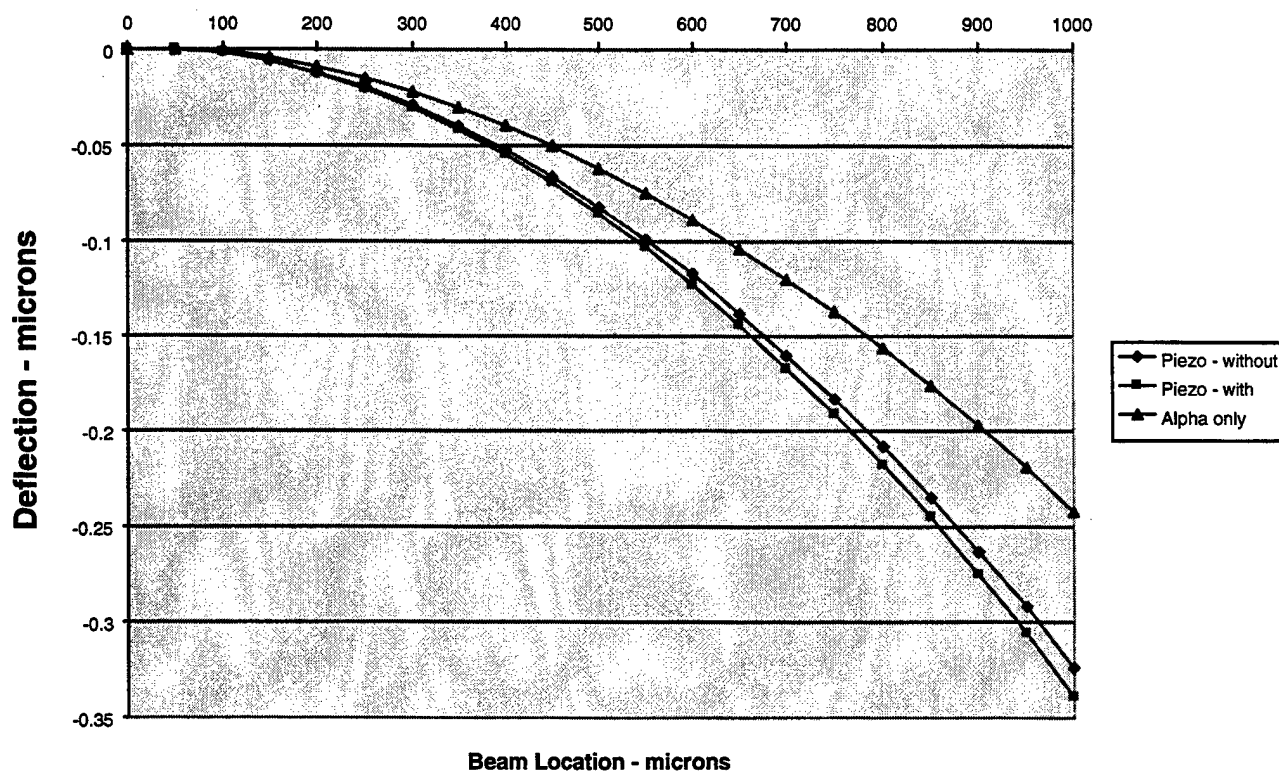

Figure 34 - The Effect of the Pyroelectric Coefficients on the Response.

In this case several result effects can be seen. The beam in all cases is subject to an enforced temperature at the cantilever base and has convection boundaries on the surfaces

to the free stream. The response in the figure represents several combinations of material properties. The curve labeled Alpha-Only shows the response of the beam as a thermal bimorph with no piezoelectric or pyroelectric coefficients. The effect is due only to the difference in the coefficients of thermal expansion of the two materials. The Piezo-without curve shows that the response increases some when piezoelectric coefficients are included. The strains produced by the thermal expansion generate a small electrical effect that increases the response slightly. The Piezo-with curve adds the pyroelectric coefficients. It shows that an additional increment of response is obtained due to the strains causing an additional electrical effect.

The following cases are typical of the types of actuator designs that were analyzed and give an idea of the model sizes used to represent the various designs as well as what sort of performance was obtained on the PC. Certainly the run times are longer than they would be on a large workstation or mini-computer, however, they are within reason for an engineer working at his/her PC. These times were obtained on a 90 MHz Pentium Gateway machine. Current technology machines with Pentium II processors and 233+ MHz would obviously be much faster.

The first case, illustrated Figure 35, is a thermal bimorph made of copper and nickel. It has a vertical step in the middle as well as a Ruthenium stop at the end that provides an anchor point for the expanding nickel to push against as it heats up.
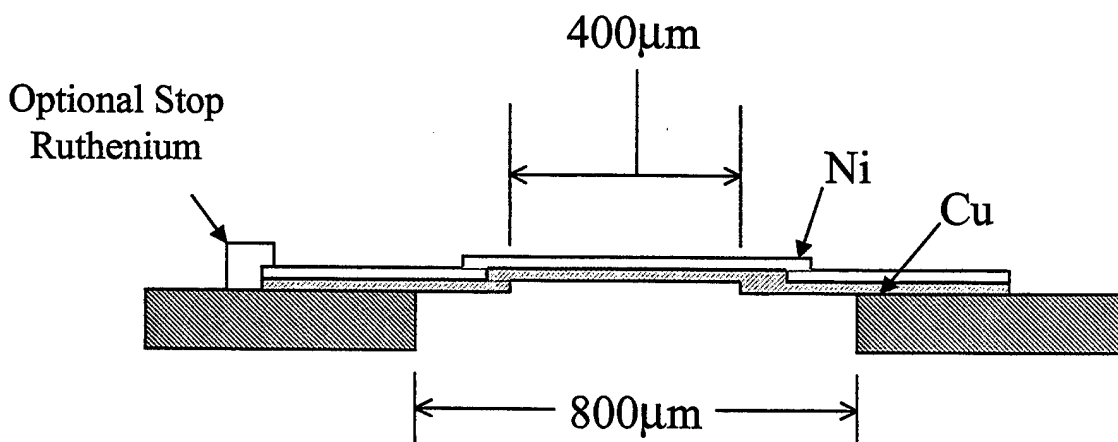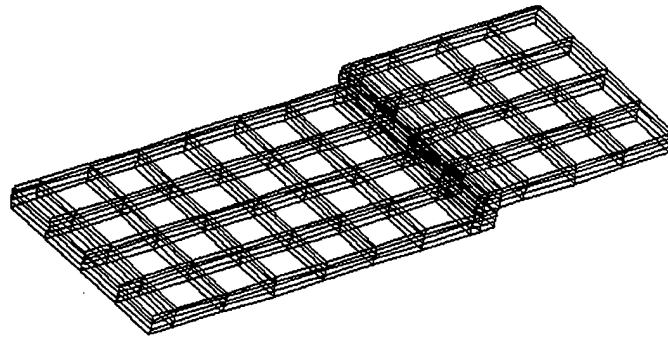

Figure 35 - Thermal Bimorph Actuator with Step.

The symmetric boundary conditions allowed the actuator to be represented by a half model. Note that the optional stop is present on both ends of the actuator. The model consisted of 410 nodes and 240 elements. This resulted in 1160 unconstrained degrees of freedom and a matrix semi-bandwidth of 167. The mesh is shown (for the half model) in Figure 36.

Thermobimorphbeamtest.File:HAAKE7.DATCornerw/stopnolip

Figure 36 - Thermal Bimorph with Step Half Model.

The run time for this case was 5 minutes and a maximum deflection of 1.3 microns was obtained at the center of the actuator. Force output for the actuator was not determined due to the small deflection value that made the design less desirable.
Another concept for a third axis actuator was the beam bender design that was developed by MCNC. This concept uses nickel dog-bone actuators to bend a cantilever section of silicon that carries the optical fiber. Figure 37 shows the design concept.
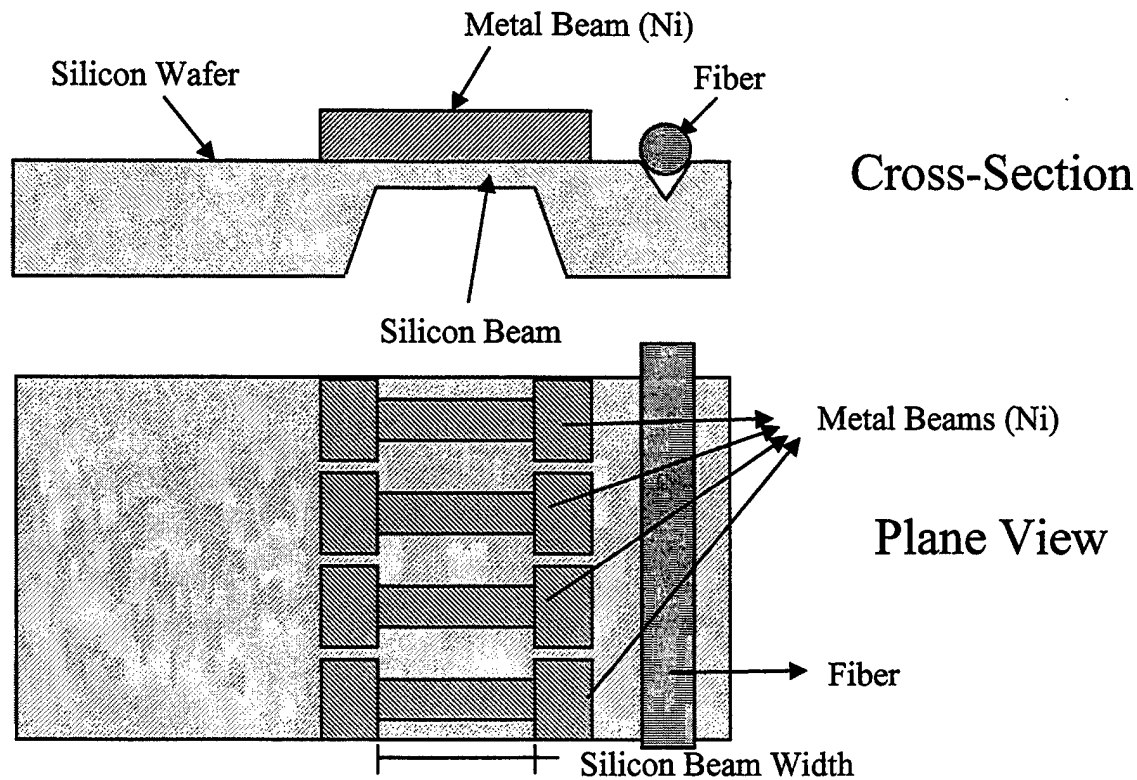
Figure 37 - Beam Bender Concept for Third Axis Alignment.

The boundary conditions in this design required that a complete cross-section model be used, however, only one actuator strip was used. The finite element mesh consisted of 1548 nodes and 776 elements. There were 3549 unconstrained degrees of freedom and a semi-bandwidth of 203. The solution time for the problem was 22 minutes. This is considerably longer than the previous case, however, still within the realm of reasonable. A plot of the mesh is shown in Figure 38. The results indicated a vertical deflection of 6.7 microns at the centerline of the optical fiber.
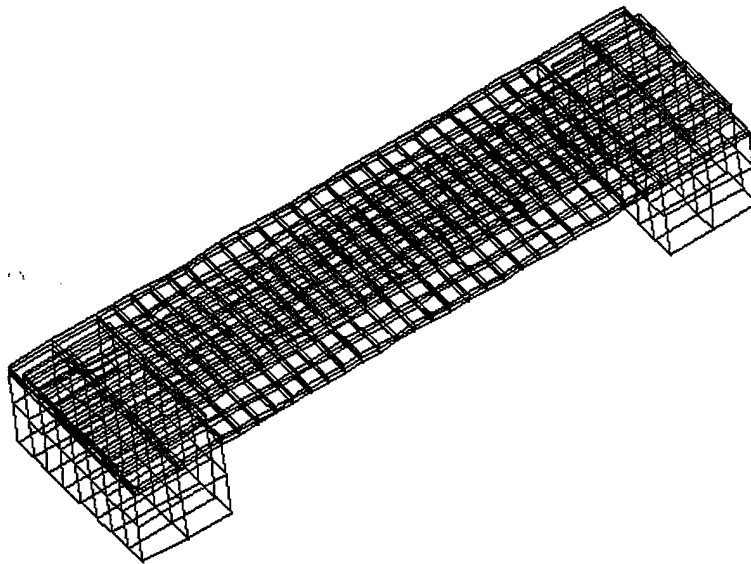
MCNCThermalBimorphActuater.File:MCNC_05.DAT

Figure 38 - Finite Element Mesh of the Beam Bender Concept.

In considering the thermal bimorph beams discussed thus far, it may be noted that the tendency for the nickel to expand is restrained by its physical attachment to the silicon base. The final concept that is discussed here is unique in that the nickel actuator is raised from the silicon beam and therefore free along its length. Attachment pads are present at both ends. The nickel is heated by passing electrical current or through the use of a heater that lies between the nickel and the silicon base. The heater tends to heat both the silicon and the nickel, thus the joule heating from the electrical current is the favored method. A detailed schematic of the actuator design is shown in Figure 39.

One of the problems that presented itself in this case was a result of the raised actuator and had not been a consideration in the previous designs. This was buckling of the actuator as it attempted to expand against the resistance of the silicon to bend. As can be seen, the nickel actuators are quite small and it was unknown under what circumstances they would merely buckle.

The analysis code is linear, thus neither buckling, nor any other failure mechanism, is accounted for in the analysis process. A process was developed that would allow for the evaluation of the level of force output from the actuator and at the same time determine the force limit that would result in buckling of the actuator.
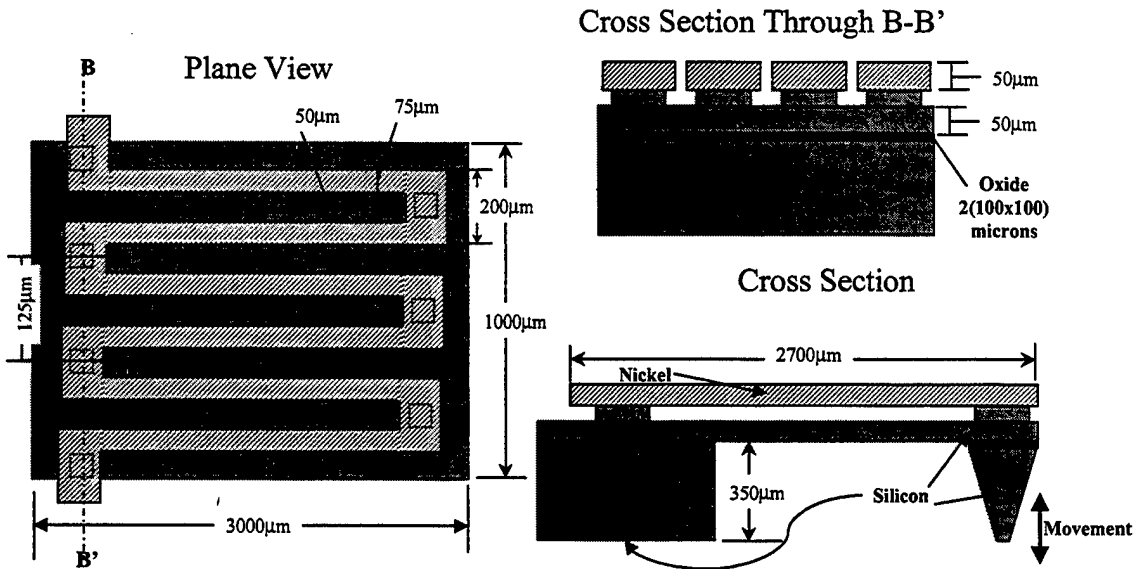
Figure 39 - Raised Actuator Design.

Again, only a single actuator beam is modeled, however, a full cross-section model is used due to the cantilever boundary conditions. The analysis code allows the use of linear spring elements. These were used in the model to attach the movement end of the actuator to ground. A variety of spring stiffnesses was used to determine the force capability of the actuator. At some point, however, the nickel actuator was going to buckle, so the full level of force available would be limited by the buckling of the nickel. The following process was used to determine the buckling cutoff for each of three different designs.

First the critical buckling load for a column of the same dimensions as the nickel actuator was computed. This axial load was used to determine the total axial deflection of the actuator under the critical load.

Second, the free expansion of the actuator was determined for the temperature increase (100C) that was used in the finite element analysis.

Third, the amount of the critical deflection was subtracted from the free thermal deflection of the actuator to determine the minimum expansion that the actuator could sustain in actual operation before it would buckle. This value is labeled the "Buckling Cutoff" on the charts we show later illustrating the deflection of the actuator for various resistive springs.

It is important to keep in mind that in the finite element model an average axial deflection of the actuator that is LESS than the buckling implies that there is an axial restraining force greater than the critical buckling load, thus the actuator is in a buckled state. If, on the other hand, the average axial deflection of the actuator is GREATER than the buckling cutoff then the axial restraining force is less than the critical buckling load and so it will not buckle.

Figure 40 shows a portion of the mesh used in the problem and a schematic of a slice with a silicon base and a raised nickel actuator. Figure 41 shows an overall view of the entire mesh just to provide some perspective on the relative dimensions of the length and height of the actuator.
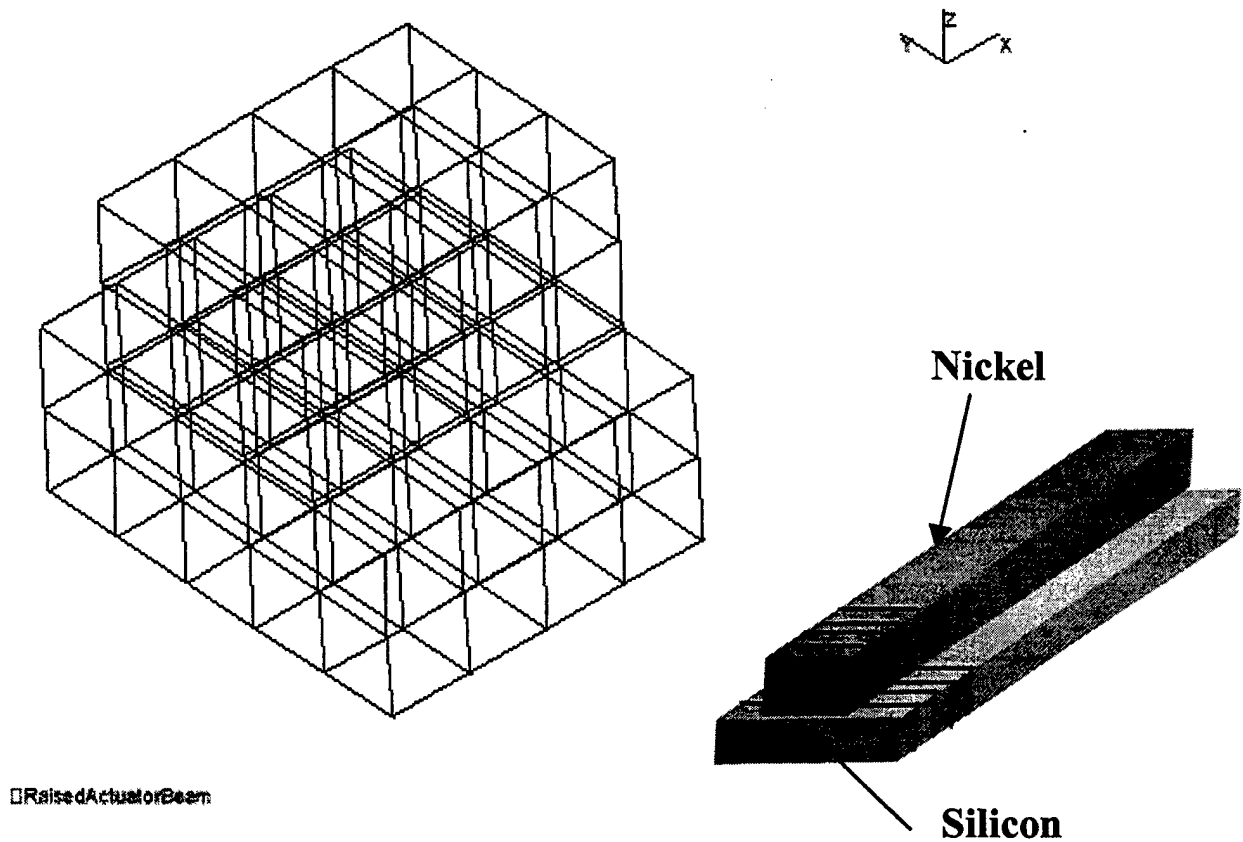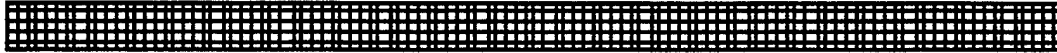

Figure 40 - Schematic of actuator model and portion of finite element mesh.

56

□RaisedActuatorBeam

Figure 41 - Total FEM mesh showing length to width of actuator model.

As one would imagine, if the stiffness of the resistive springs increases, the deflection of the actuator goes down. Three actuator designs were modeled. These contained different sized nickel actuators. The baseline design was a 75 x 50 micron cross-section nickel actuator where the 75 micron dimension was the width of the beam and remained the same in each case. The second was a 75 x 75 micron cross-section nickel actuator, and the third was a 75 x 100 micron cross-section.

Several points are worthy of note about these designs. First, as the cross-section of the nickel increased, you would perhaps expect a greater force capability due to the larger quantity of nickel to expand, and you would expect that there would be a smaller chance of it buckling due to the larger cross-section. Second, and perhaps unexpectedly, the free deflection of the actuator is smaller for the larger nickel. This results from the greater bending stiffness of the overall nickel/silicon piece. The following figures give the details of the response of the actuator.

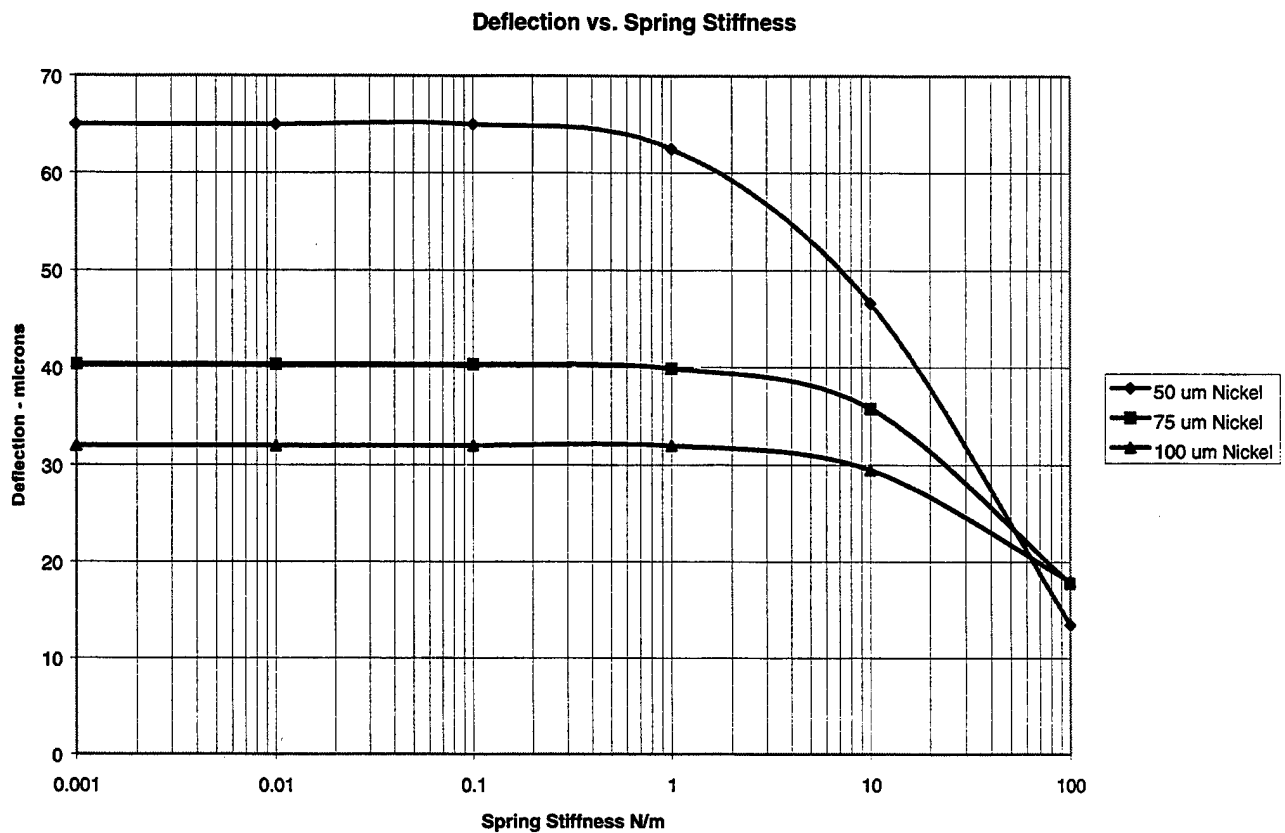**Deflection vs. Spring Stiffness**

Figure 42 - Deflection of the three actuator designs with varying resistive springs.

As can be seen in Figure 42, the deflection of each actuator decreases as the resistive springs increase. Note that all three have approximately the same deflection when a 60 N-m spring is used. The larger nickel cross-section results in less free deflection, as mentioned above.
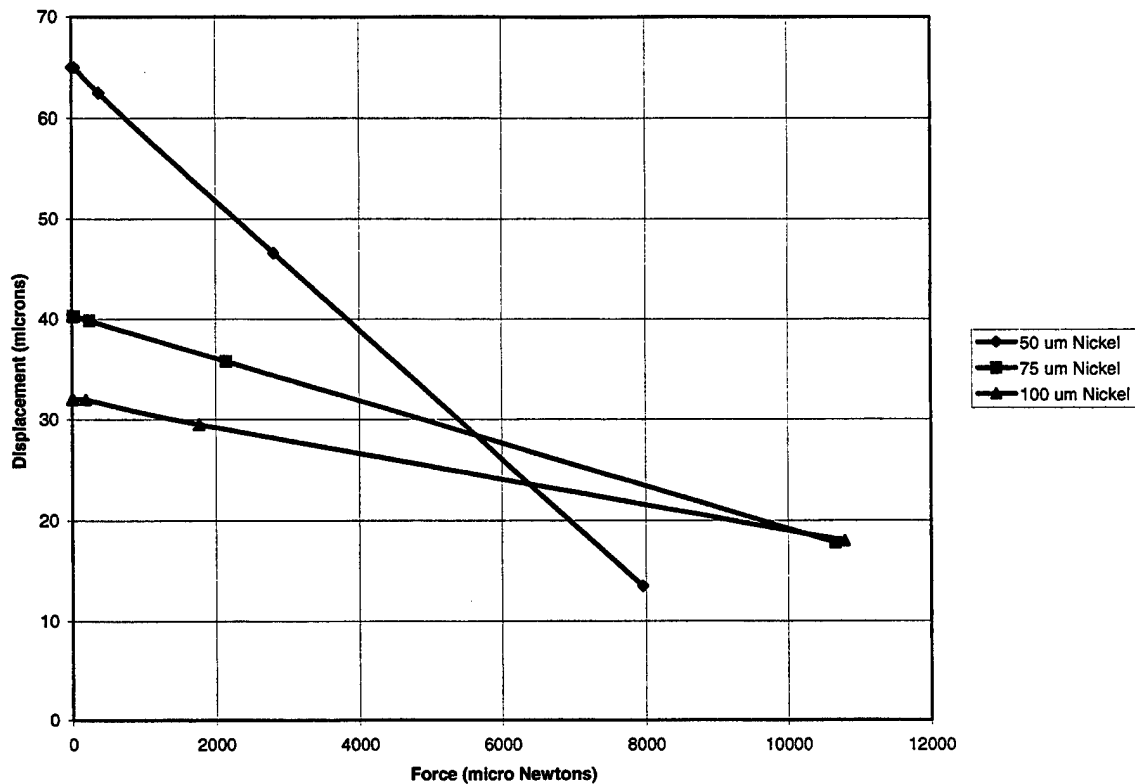
Figure 43 - Actuator force output at various displacement conditions.

In Figure 43 we see clearly that the force output of the actuator increases as the delfection of the actuator is restricted by stiffer resistance springs. This is again as you would expect. The question about the buckling of the actuator, however, remains. If the actuator buckles at some point, the this represents the limiting value of force and the full value indicated in Figure 43 may not be attained. To clarify the buckling cutoff effects the following two figures show the deflection of the actuators along with their respective cutoff values. It should be noted that the 75 and 100 micron actuators share the same these designs, and thus their buckling load is the same. These two are shown on the same cutoff. This is due to the fact that 75 microns remains the smallest dimension in both of these designs, and thus their buckling cutoff is the same. These two are shown of the same plot. Notice in that the 50 micron actuator is well below the cutoff indicating that it will buckle prior to moving the beam at all. It is therefore completely ineffective. Figure 45 shows that both of the other designs are above the buckling cutoff until a resistive spring of approximately 100 N/m is used. The 100 N/m springs correspond to a displace for both of the actuators of approximately 18 microns (Figure 42) and a resulting force limit of approximately 10,000 micro-Newtons (Figure 43).
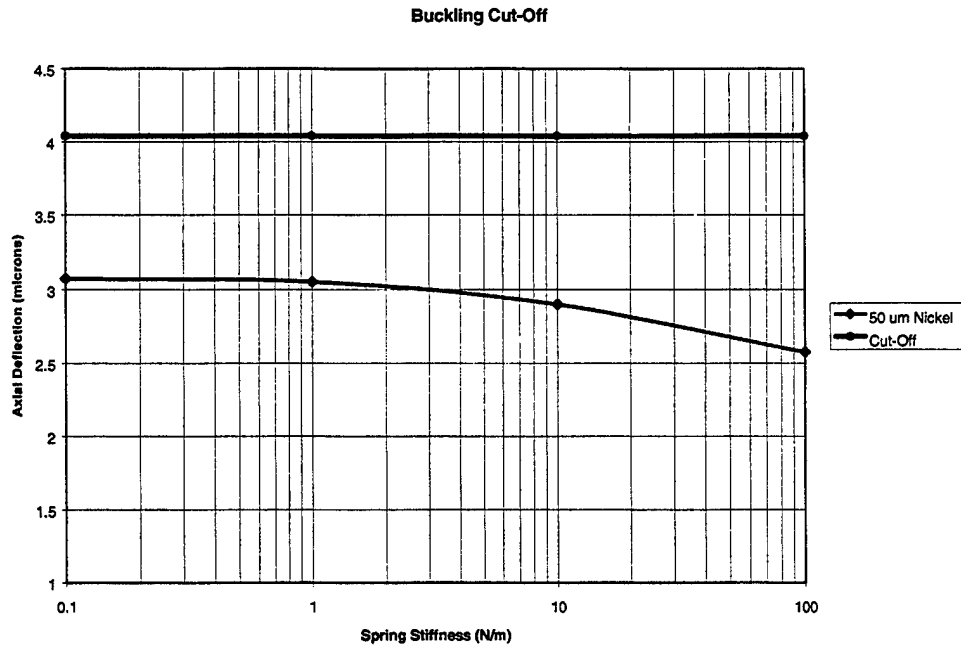
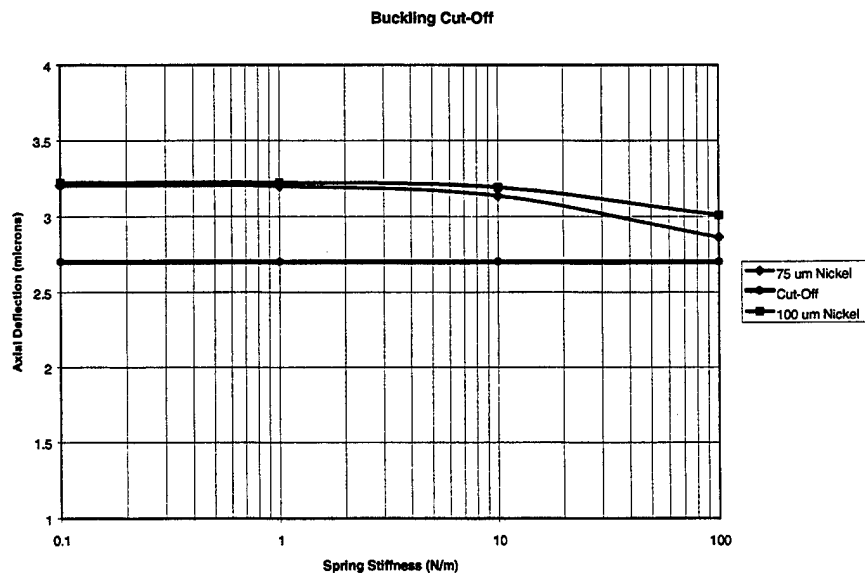**Figure 44 - Deflection of 50 micron actuator actuators with buckling cutoff.**

Figure 45 - Deflection of 75 and 100 micron actuators with buckling cutoff.

60

FEM Summary

The analysis code, as developed, achieves the AMPS program design goals including coupling thermal, electrical, and mechanical analysis. It provides the ability to analyze a large class of state-of-the-art problems while requiring only a PC well within the description of the "standard" machine that is available in the marketplace today. The executable, by virtue of the allocatable memory scheme, is small and yet large problems can be solved. The code chooses the most efficient storage method, for the particular problem under consideration, which results in reasonable run times even for very large problems. A wide variety of constraint and "loading" options are available, allowing the representation of real design cases.

There are some areas for potential improvements, such as nonlinear material behavior and fully coupled transient response, which would add some nice features to the analysis method. The present code is, however, a step forward in the ability to study the design of micro-electro-mechanical structures.

List of all Publications and Technical Reports

Austin Tx, 1997   Micromaching and Microfabrication '97
John M. Haake, Robert L. Wood, Vijayakumar R. Duhler, Howard R. Last, "Direct Measurement of Force and Displacement of LIGA Micro Springs and Actuators", *Proceedings of SPIE* Vol 3225-20. Presented as Late paper. Not published

Photonics West '98
J. M. Haake, R.L. Wood, and V. J. Duhler, "In-package active fiber optic micro aligner", *Proceeding of SPIE* vol. 3276-20.

SPIE's 1998 SMART STRUCTURES AND MATERIALS SYMPOSIUM
Edward V. White[1], Mark D. Rogers[1], and John M. Haake[2] "Three Axis Micro Actuator For Smart Optical Interconnect System" , Proceeding of SPIE Vol 3328-38, To be published

ECTC - Electronic Components and Technology Conference Optoelectronics- Seattle WA
Poster Paper # 147
J.M. Haake, "In Package Micro Aligner for Fiber-Optic Packaging", *Proceeding of ECTC,*

List Of All Participating Scientific Personnel Showing Any Advanced Degrees Earned By Them While Employed On The Project

Haake, J., Smith, H., O. Auciello, R. Wood, B. Augustine, V. Dhuler

Report on Inventions (By Title Only)

"A Microactuator For Precisely Aligning An Optical Fiber And An Associated Fabrication Method" - **Patent # 5602955**

"Multiple GRIN Lens Coupled Active Fiberoptic Connector" - **Patent # 5606635**

"Internally referenced Microactuator For Precisely Aligning An Optical Fiber And An Associated Fabrication Method" - **Patent Pending**

"Micromanipulator for precisely aligning guide wave devises and an associated Fabrication Method" - **To be filed**

Bibliography

1. Haber, L "Opto-electronic bets on low cost", Lightwave, Feb. 1995
2. NIST Internal Report 5715, "Optoelectronics and Optomechanics Manufacturing: ATP Focused Program Development Workshop Proceedings", Feb. 15, 1995
3. Optoelectronics Industry Development Association (OIDA) "Optoelectronic Technology Roadmap", 1994
4. G. Kotelly "Opto-electronics-high-volume, low-cost devices needed", Editorial, Lightwave, Feb. 1995
5. D.K. Probst, et al. "Demonstration of an integrated, active 4 X 4 photonic crossbar", IEEE Photonic Tech. Lett. 4 [10] 1139-1141 (1992)
6. C. L. Balestra, "Implementation of integrated optic system with active waveguides, passive waveguides, and optical fibers", International Conference on Applications of Photonic Technology, Toronto, June 21-23, 1994
7. J. M. Haake and Russell T. Fairles, "Development of a fiber optic interferometer demodulation / multiplexing system using an active 1 X 10 photonic polarization preserving fiber coupler", SPIE-Smart Structures Conference, 1918-54, 1993
8. J.M. Haake and Bartley Johnson, "Implementation of an active AlGaAs based 1X10 photonic polarization preserving fiber coupler in a fiber optic sensor demodulation system", SPIE - Smart Structures and Materials Conference, 2448-22, 1995.
9. P. Ayliffe, et al., "The hybrid integration of optical electronic components on silicon", International Journal of Optoelectronics, 1994, vol. 9, No 2, pp. 179-191
10. Edmond J. Murphy, "Fiber attachment for guided wave devices", Journal of Lightwave Technology, Vol. 6 No 6 June 1988
11. Chaoui et al. , "An isolated laser module based on modularity concept", 1991 Electronic Components and Technology Conference, IEEE
12. Presby, H. M. and C.A. Edwards, "Near 100% efficient fibre microlenses", Electronic Letters, 3/12/92, Vol. 28 No. 6   U.S. Patents 4,932,989, 5,011,254, and 5,256,851
13. C.A. Edwards and H.M. Presby, "Coupling-sensitivity comparison of hemisphere and hyperbolic microlenses", Applied Optics, Vol. 31., No. 9.
14. Scott Enochs, "Opto-mechanical stability of a laser diode module with soldered fiber", 7th Annual International Electronics Packaging Conference, Nov 1987.
15. M.S. Cohen, et al., "Packaging of high density fiber/laser modules using passive alignment techniques", 1992 Electronic Components and Technology Conference, IEEE
16. O.T. Strand, et al., "Automated fiber pigtailing technology", 1994 IEEE 44th Electronic Components & Technology Conference (ECTC) - IEEE
17. Oliver t. Strand, "Low-cost automated fiber pigtailing machine", 1996 Electronic Components and Technology Conference, IEEE
18. Erik C.M. Pennings, "Challenges in optoelectronic packaging of high performance WDM networks", 1997 ECTC, IEEE
19. H. P. Hsu, A.F. Milton, "Flip-chip approach to endfire coupling between single-mode fibers and channel waveguides" Electron Lett., vol. 12, pp. 404-405, 1976
20. H. P. Hsu, et al., "ARPA analogue optoelectronic module program: packaging challenges for analogue optoelectronic arrays", 1995 ECTC - IEEE
21. Lutz Weber, et al., "Micro-molding – a powerful tool for the large scale production of precise microstructures", SPIE Vol. 2879
22. Michael J. Wale, Colin Edge, "Self-aligned flip-chip assembly of photonic devices with electrical and optical Connections", IEEE Transactions on Components, Hybrids, and Manufacturing Technology, Vol. 13, No. 4, Dec. 1990
23. J. Sutherland, et al., "Optical coupling and alignment tolerances in optoelectronic array interface assemblies", 1995 ECTC – IEEE
24. J. Sutherland, et al., "Alignment tolerance measurement and optical coupling modeling for optoelectronic array interface assemblies", 1996 ECTC – IEEE
25. Thomas Frank, "Development and manufacturing of a two-dimensional microactuator for moving an optical fiber", SPIE Vol. 2882

26. Scott D. Collins, et al. , "Microfabrication creates mesoscopic optical Systems", Laser Focus World may 1997

27. Peter Krulevich, et al., "Thin film shape memory alloy microactuators", Journal of Microelectromechanical Systems, Vol. 5. No. 4 Dec. 1996

28. R. Jebens, et al., "Microactuators for aligning optical fibers", Sensors and Actuators, 20 1989 pp. 65-73

29. Leslie A. Field, et al., "Micromachined 1X 2 optical-fiber switch", Sensors and Actuators A53, 1996 pp. 311-315

30. U.S. Patent 5,080,458

31. Yokio Kikuya, et al. "Alignment of optical axes by using electrostatic force", Optics Letters Vol. 18 No. 11, June 1, 1993

32. Shin'ichi Aoshima, et al., "Compact mass axis alignment device with piezoelements for optical fibers", IEEE Photonic Technology Lett., Vol. 4, No. 5, may 1992

33. David Craven, et al., "Anisotropic high-aspect ratio etching in a high-density plasma", SPIE Micromachining and Microfabrication 1995.

34. J. M. Haake, R L. Wood, V. R. Duhler, H. R. Last, "Direct Measurement of Force and Displacement of LIGA Micro Springs and Actuators", - Unpublished

35. F.P. Beer and E.R. Johnston, Jr., *Mechanics of Materials*, 1981, McGraw-Hill

W.D. Pilkey and O.H. Pilkey, *Mechanics of Solids* 1974, Quantum Publishers

Appendix

Appendix A - Optical Design Considerations

Singlemode Fiberoptic Connectors

There are two general methods to make an optical connection. The first and most commonly used is the "Butt coupled" method. The second is lensed fiberoptic collimated connector method.

Butt Coupling Configuration

This is the simplest system to model since there are no lenses and the two coupling modes are identical. Using a standard telecommunication fiberoptic with a transmission wavelength of 1.3 μm , the optical mode radius at the e^{-2} power points is approximately 5.6 μm. (11.2 μm dia.). The other plotted line is typical for a GRaded INdex (GRIN) lens in a butt coupled configuration with a mode radius of 100μm. As shown by the graphs in Figures 1, 2, and 3, the butt coupled single mode fiberoptic system is insensitive to angular tilt but sensitive to linear displacement. In all these graphs which are from a MathCad file the vertical axis is normalized coupling efficiency.
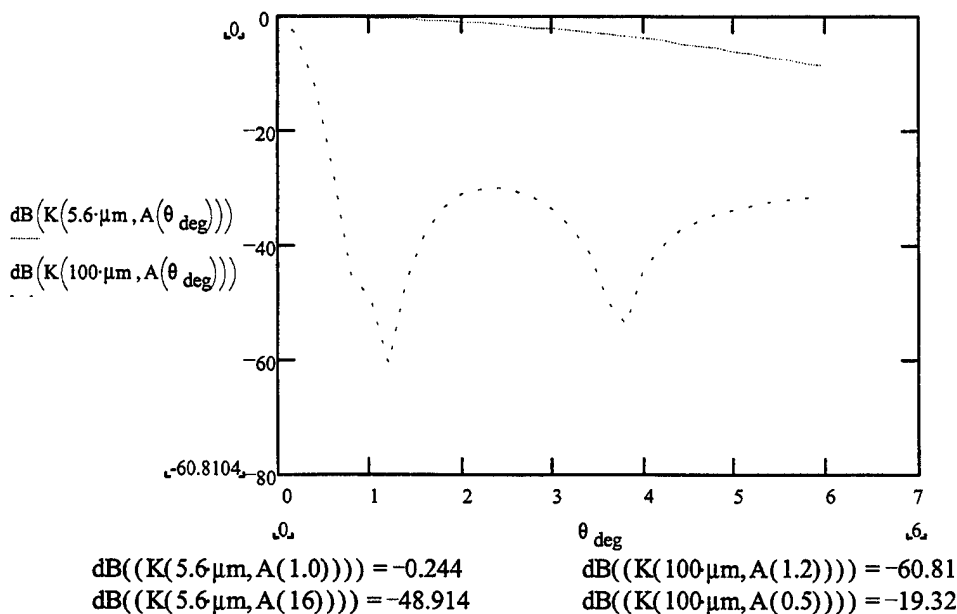

$$dB((K(5.6\,\mu m, A(1.0)))) = -0.244 \qquad dB((K(100\,\mu m, A(1.2)))) = -60.81$$
$$dB((K(5.6\,\mu m, A(16)))) = -48.914 \qquad dB((K(100\,\mu m, A(0.5)))) = -19.32$$

Figure 1. Tilted Guassian mode of the same size. Radii of 5.6 μm and 100μm. (Note: that the optical tilt is twice the angle polished onto the optical surface)

In a typical single mode fiber optic connector the fiberoptic is first placed in the ceramic ferule and the entire ferule with fiberoptic is polished with a angle of 8 degrees (16 degrees optically) this yields a feedback return loss of approximately 49 dB. The optical angle is twice the polish angle due to the fact that the light leaves the fiber is reflected off a external object and couples back into the fiberoptic, thus goes through two tilts of equal angular offsets.

1

$K(5.6 \cdot \mu m, \text{Displacement})$

$K(100 \cdot \mu m, \text{Displacement})$
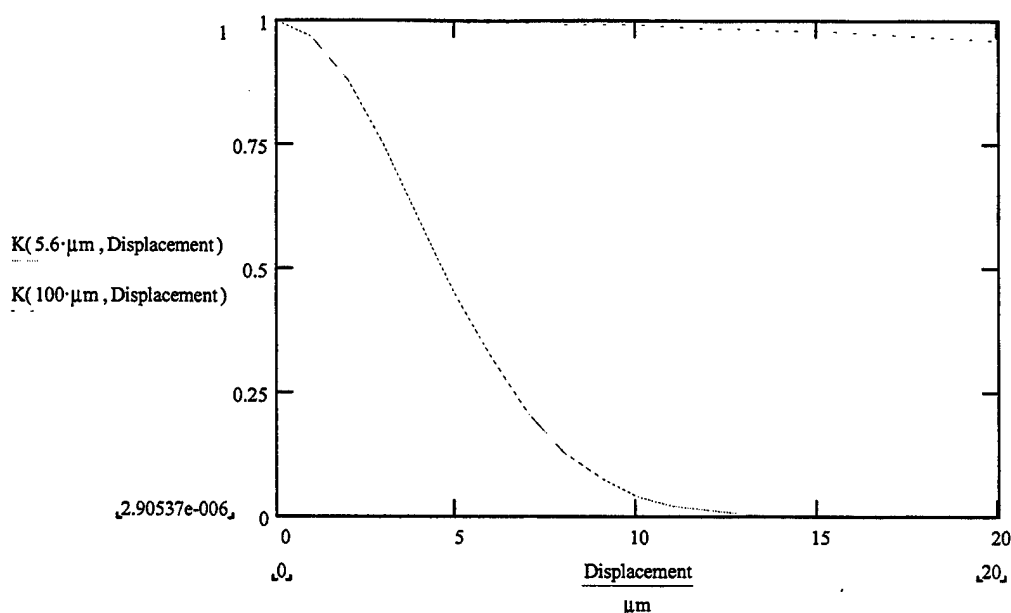
$dB(K(5.6 \mu m, 1.9 \cdot \mu m)) = -0.499$

$dB(K(100 \cdot \mu m, 34 \mu m)) = -0.501$

Figure 2 Displaced Guassians of the same size

$dB(K(5.6 \cdot \mu m, 5.6 \cdot \mu m, z))$
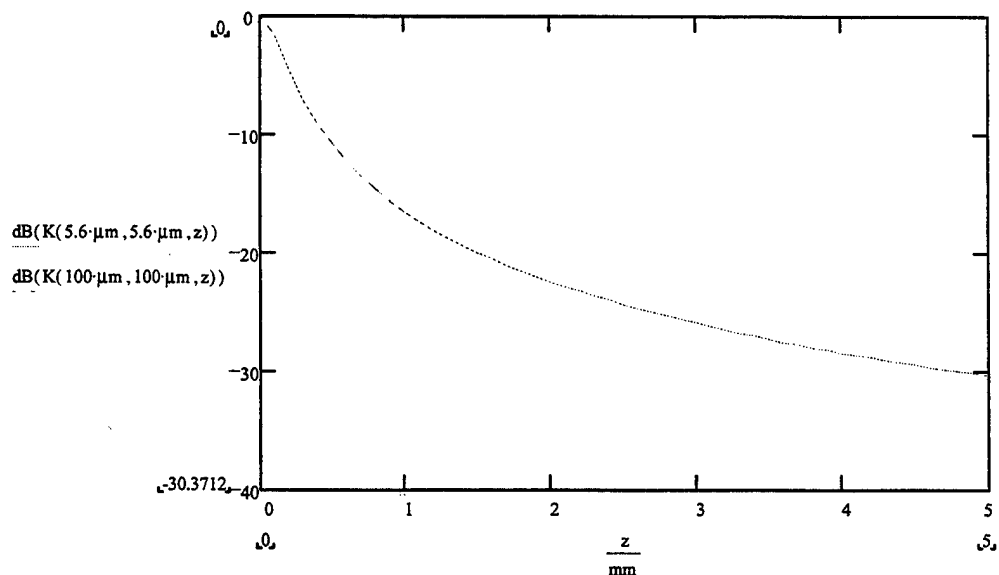
$dB(K(100 \cdot \mu m, 100 \cdot \mu m, z))$

$dB(K(5.6 \mu m, 5.6 \mu m, 100 \mu m)) = -1.572$ $dB(K(100 \mu m, 100 \mu m, 30 \cdot mm)) = -1.418$

Figure 3 Normalized coupling efficiency between two modes of the same radii with respect to displacement along the optical axis (Z mm).

In Figure 2 it can be seen that the butt couple fibers are very sensitive to linear offset that are orthogonal to the optical axis. A 1.9 μm displacement translates into a 0.5 dB loss. This is actually very tolerant and this is the another reason why so many systems are driven toward the longer wavelengths. This is on top of the fact that there are long distance transmission windows for fused silica at 1300 and 1550 nm. If one want to use silicon detectors and GaAs based devices at 900nm were the core radius is 3μm the tolerance to movement is approximately cut in half as shown in Figure 4 below.

2

Displacement $:= 0, 0.25\cdot\mu m .. 5.0\cdot\mu m$
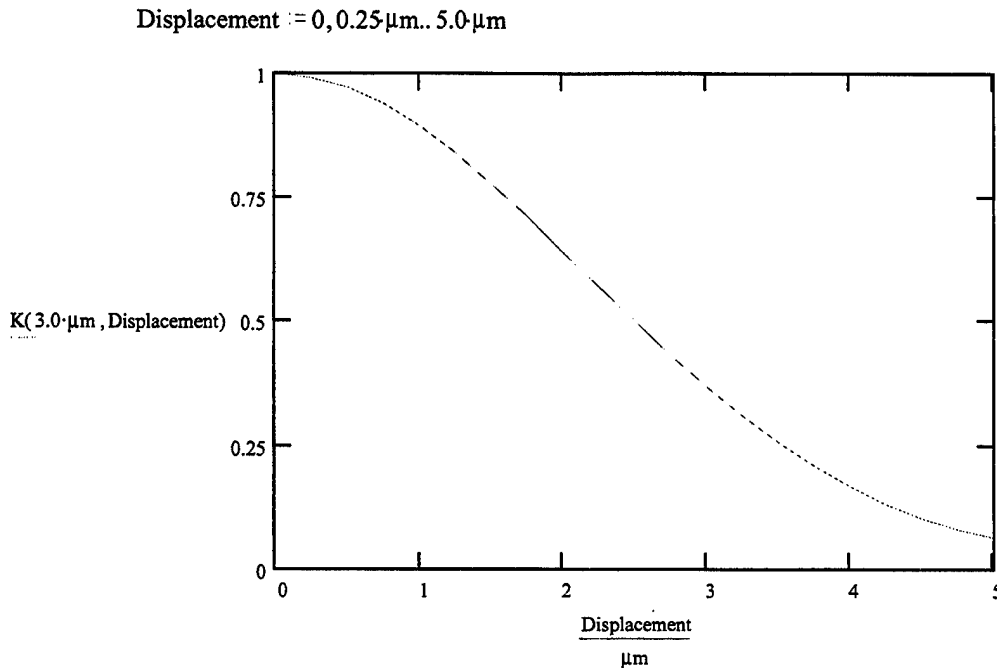
$dB(K(3.0\cdot\mu m, 1.0\cdot\mu m)) = -0.481$

Figure 4 - Displaced Guassians of same size (mode radius = 3.0μm)

Advantages and Disadvantages

The butt coupled fiberoptic connector advantages are:
1. Contains only two optical components
2. Requires no special mode matching optics since the optical components are identical
3. The small mode size has a very large angular tolerance

The disadvantages of the butt coupled connector are:
1. The small mode size has a very small linear displacement tolerance range
2. The small mode size requires a very large angle (8 degrees) to be polished onto the facet to prevent feedback
3. The small mode size in susceptible to dirt contamination

Lensed Fiberoptic Collimated Connector

In this design, the AMPS microactutor is used to align a fiber to a GRaded INdex (GRIN) lens. The lens will expand the beam from a fiber and collimate or create parallel rays which will not disperse in a gap. Another lens facing the first will capture the rays and refocus them onto the next fiber, creating a fiber optic connector. This type of design allows for almost lossless insertions and extractions over hundreds of cycles due to the noncontact formation of the lenses during operation and the robustness due to the large surface area of the lenses. This contrasts with the more typical butt coupled (point contact) approaches where surface damage and degradation can occur due to particle obstruction and coupling losses occur due to axial separation.

Due to the basic laws of physics you cannot get something for nothing, therefore there are some disadvantages to going to a larger beam. Marcuse [1] described the canonical relationship between beam size and its tolerance to angular and linear displacement. He call it the uncertainty principle. As you drive the beam diameters up to make them insensitive to linear misalignment the angular misalignment tolerance becomes extremely small. And vice versa. When you drive the beam diameters to be small to make them insensitive to angular misalignments the linear misalignment tolerances become extremely small.

3

Therefore, there is a region of beam diameters to be designed is solely determined by the manufacturability and the environment in which the optical connector has to function. A determination of the best mode size to design to will be learned from the fabrication and use of these active connectors. With this preliminary design only off the shelf GRIN lenses will be used.

In Figure 5 a typical optical schematic is shown. An optical fiber is aligned to a 0.25 pitch GRIN lens [2] which collimate the light coming form the fiber. The actual optical mode radius of exiting the GRIN is much smaller than the manufactured radius of the GRIN.
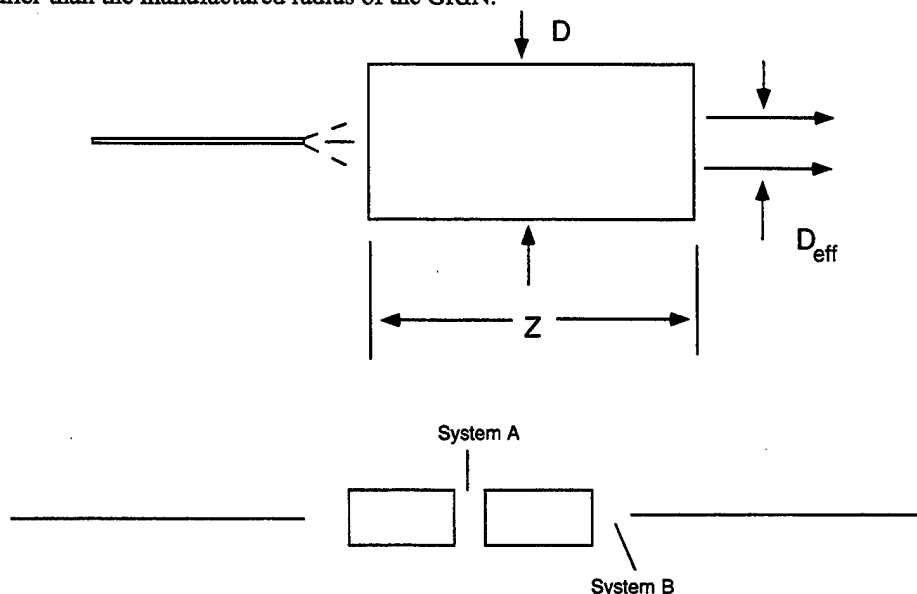

Figure 5 Optical schematic layout of a GRIN / Fiberoptic Collimating system

Grin Lens specifications: SELFOC Product Guide

Type **SLS-1.0-0.25-A2-1.30-M- XX**

SLS   Standard Numerical Aperture = 0.37

1.0   1.0 mm in diameter = D

0.25   Pitch is 0.25   This defines the length $Z=2\pi P/A^{-2}$

A2   Anti-Reflective Coated $@\lambda$

1.30 λ = 1300 nm

M   Metallization

XX   Angle Facet Specification (none)

Optical System A GRIN-GRIN

The effective optical diameter (D_{eff}) of the of the GRIN after collimation is approximately 200 • m. With the effective radius of 100 • m, the sensitivity to angular and linear displacements are shown in Figure 1-3. In Figure 1 it can be seen that the GRIN is six orders or magnitude more sensitive to angular displacement than the butt couple fiberoptic. In Figure 2 the GRIN to GRIN coupling is less sensitive to linear movement off the optical axis (X, Y) by approximately ratio of the radii (100/5.6 = 17.85). In Figure 3 this system is less sensitive to movement along the optical axis (Z) by the ratio of the radii squared (17.85^2 = 318).

One of the big concerns with multiple optical elements is reflection which can feedback into the transmit fiber. As discussed above, one of the techniques used by the telecommunication industry is to polish the

4

fiber facet with an angle of 8 degrees. The GRIN lens shown here has a mode field radius of 100 µm. As can be seen in Figure 1 the optimum angle to have polished onto the end of the GRIN is 1.2/2 degrees, or 0.6 degrees. The manufacture has a option for angle facet but their angle are unnecessarily large (2,4,6,8 degrees), and as can be seen from Figure 1, nothing additional is gained from the larger angles. *The artifacts after 1.2 degrees are real and are related to the function.*

One of the preliminary fabrication steps involved with manufacturing a connector is the polishing of the entire mating surface after the GRIN lenses are mounted in the package wall. Some optical material will be removed. The change in the coupling efficiency of an optimized GRIN connector as one connector is polished back (i.e. GRIN lens is shortened) is shown in Figure 6.
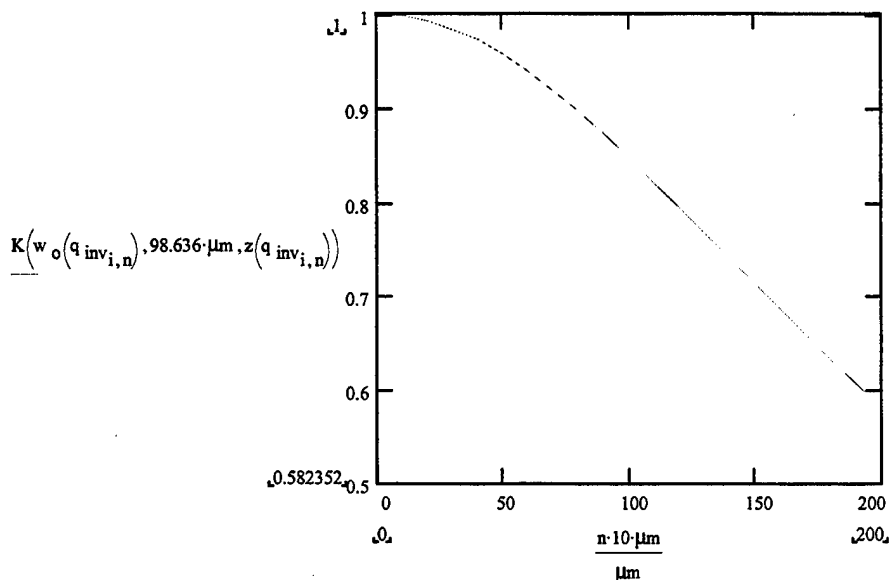

Figure 6 The change in normalized coupling efficiency in a previously optimized System A as the GRIN is polished back.

Optical System B Fiber-GRIN

The optical system B is the system which will require micro to submicron alignment of the fiberoptic to the grin lens in the linear axis (X, Y). The GRIN lens translates a linear movement of the input beam into a pure angular tilt on the output. Using this fact a plot of the linear offset versus coupling efficiency is made in two plots in Figure 6. This system is very insensitive to movement in the Z axis. The 0.25 GRIN lens is a phase front transformer. It will take a diverging beam from a point source (i.e. the fiberoptic) and transform it to a collimated beam of the same waist size (D_{eff}) as long as the GRIN remains under filled. This implies that the fiberoptic can be positioned within several millimeters range in the Z axis in front of the GRIN lens. This system is also very insensitive to angular misalignment since this is translated to a linear offset at the GRIN output.

5

$$dB\big(K\big(100{\cdot}\mu m, A\big(\Delta_x\big)\big)\big)$$
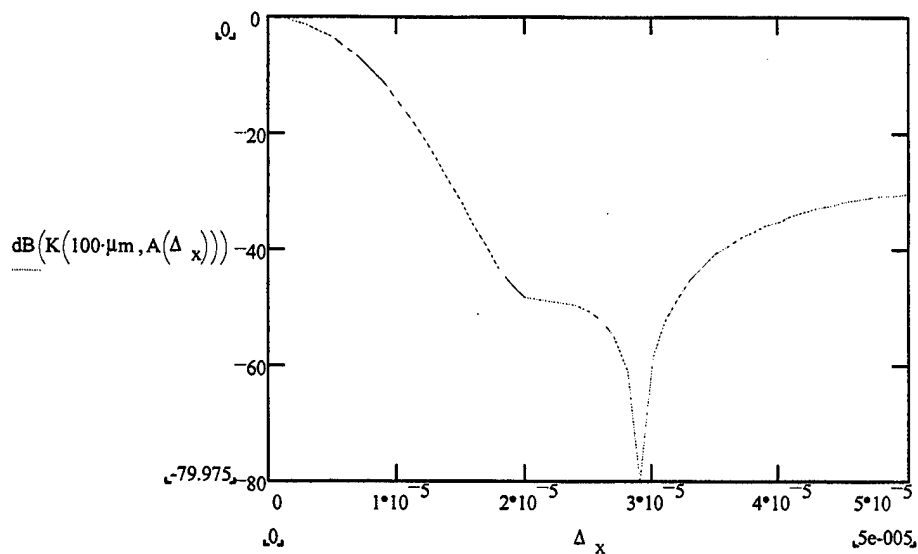
A. Displacement of the Fiberoptic Off Axis

$$dB\big(K\big(100{\cdot}\mu m, A\big(\Delta_x\big)\big)\big)$$
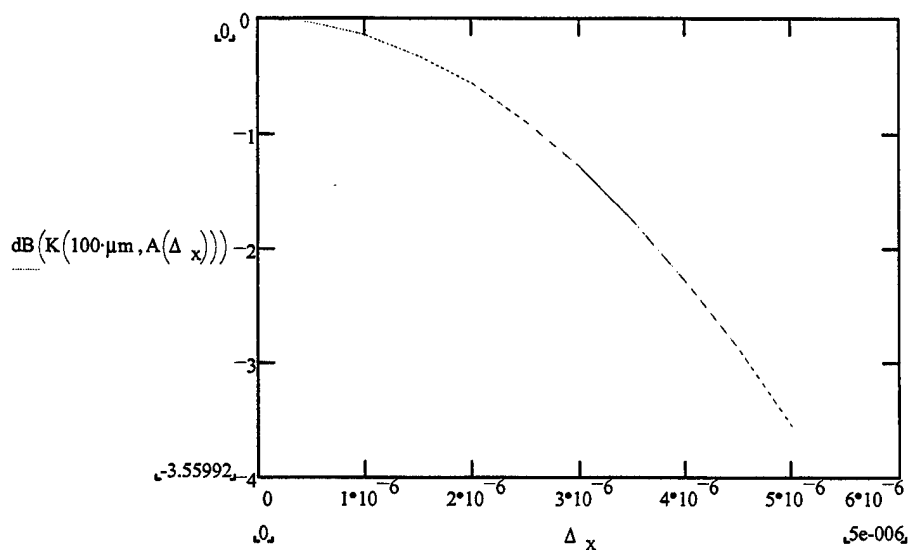
B. Displacement of the fiberoptic off axis between the 0 and 5 μm.

Figure 7 Normalized coupling efficiency versus linear displacement of the fiberoptic in X & Y axes for optical system B.

Advantages and Disadvantages

The GRIN lens connector offers unsurpassed performance at the output.

* The Advantages are:

1. Large mode size has very large tolerances in the linear directions
2. Large mode size is immune to dirt contamination
3. The output surface is planer therefore field cleanable
4. The angle to be polished onto the output is very small to get a very large isolation to feedback reflections

* The disadvantages of the GRIN connector are:
1. The large mode size has a very small angular tolerance
2. The connector contains multiple optical elements (4) which implies six optical interfaces. More optical elements imply more chance for scatter and reflective losses.

References

[1] D. Marcuse, "Loss Analysis of Single Mode Fiber Splices", The Bell System Technical Journal, Vol. 56, No. 5, May-June 1977
[2] SELFOC Product Guide SPG-390-M2M, Nippon Sheet Glass